

## SUPPLEMENTARY INFORMATION

## Supplementary Information A fast, robust and tunable synthetic gene oscillator

Jesse Stricker<sup>1\*</sup>, Scott Cookson<sup>1\*</sup>, Matthew R. Bennett<sup>1,2\*</sup>,  
William H. Mather<sup>1</sup>, Lev S. Tsimring<sup>2</sup> & Jeff Hasty<sup>1,2,3</sup>

<sup>1</sup> Department of Bioengineering, University of California, San Diego, La Jolla, California, 92093 USA.

<sup>2</sup> Institute for Nonlinear Science, University of California, San Diego, La Jolla, California, 92093 USA.

<sup>3</sup> Corresponding Author. Department of Bioengineering, University of California, San Diego, Mail-code 0412, La Jolla, CA 92093-0412, USA. Telephone: 858 822 3442. Fax: 858 534 5722. Email: hasty@bioeng.ucsd.edu.

\* These authors contributed equally to this work.

## Materials and Methods

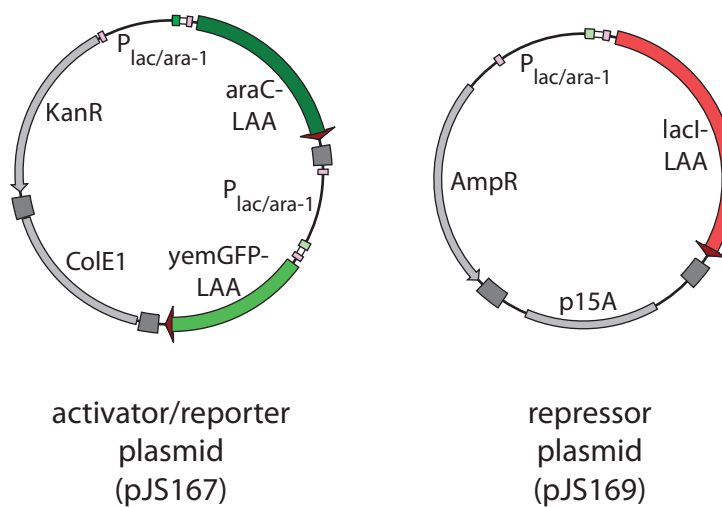
### Plasmid construction

Using a tagging vector, the two components of the oscillator (*araC* and *lacI*) and the gene encoding the fluorescent reporter protein (*yemGFP*) were tagged with carboxy-terminal *ssrA* tags (Andersen et al. 1998) consisting of **TSAANDENYALAA**. The TS sequence encodes a SpeI site and acts as a linker, while the *ssrA* tag (in bold) targets proteins to the ClpXP degradation pathway, greatly increasing their degradation rates and therefore dynamic behavior. The first codon of the *lacI* gene was changed from its wildtype sequence of GTG to a standard ATG start codon. The GFP allele used in this study contains F64L/S65T/A206K mutations and is codon-optimized for yeast expression (Sheff and Thorn 2004). The first two mutations correspond to mut1GFP (Cormack et al. 1996), while the A206K mutation interferes with GFP dimerization (Zacharias et al. 2002). The yeast codon optimization does not appear to have any effects in *E. coli* other than a mild decrease in expression. In our experience, many GFP variants have deleterious effects in bacteria, especially when expressed at high levels, which may be due to multimerization (Shaner et al. 2005). The A206K mutation allows increased GFP expression without deleterious effects (as measured by growth rate or forward scatter measurements by flow cytometry).

These three tagged genes were cloned into pZ modular plasmids under the transcriptional control of the *p<sub>lac/ara-1</sub>* hybrid promoter (Lutz and Bujard 1997) to form three coregulated transcriptional modules. The promoter, ribosome binding sequence, and downstream terminator are identical between modules. The *p<sub>lac/ara-1</sub>* promoter is activated by AraC in the presence of arabinose and repressed by LacI in the absence of IPTG. It includes two *lacO* operator sites, one overlapping and the other ~500 bp upstream of the transcription start site. LacI repression is

mediated by DNA looping by LacI tetramer bound to both sites. We found that a single point mutation in the upstream *lacO* site abolished LacI repression.

The activator *araC* module and the reporter *yemGFP* module were placed on a ColE1 plasmid with kanamycin resistance (pJS167). Although this plasmid contains repeated regions (the *P<sub>lac/ara-1</sub>* and terminator sequences), we found no evidence of plasmid instability. The repressor module was placed on a p15A plasmid with ampicillin resistance (pJS169). All PCR-amplified sections and sequence junctions were confirmed by sequencing. (See Supplementary Fig. 1.)



**Supplementary Figure 1:** The two plasmids containing the dual-feedback oscillator circuit. The activator and reporter modules are on a derivative of pZE24 (Lutz and Bujard 1997), a medium-copy (Chang and Cohen 1978) ColE1 plasmid, while the repressor module is on a derivative of pZA14 (Lutz and Bujard 1997), a lower-copy (Kahn et al. 1979; Atlung et al. 1999) p15A plasmid. Cotransformation of  $\Delta$ *araC*  $\Delta$ *lacI* *E. coli* cells with both of these plasmids gives the oscillator strain JS011. Transcriptional terminators are shown as dark gray squares. Plasmid maps were drawn with Savvy (<http://bioinformatics.org/savvy/>).

To construct the negative feedback oscillator strain, the hybrid promoter *p<sub>LlacO-1</sub>* (Lutz and Bujard 1997) was used to regulate expression of *lacI* and *yemGFP*. Both genes were tagged with *ssrA* tags as described above. The *p<sub>LlacO-1</sub>* promoter consists of the *p<sub>L</sub>* promoter from  $\lambda$  phage with *lacO* sites replacing the *cI* binding sites. The *p<sub>L</sub>* promoter gives constitutive transcription without *cI* binding. The addition of *lacO* sites allows repression by LacI in the absence of IPTG. Two transcriptional modules containing *p<sub>LlacO-1</sub>* and *lacI* or *yemGFP* were constructed as above. The repressor module was placed on a p15A plasmid with chloramphenicol resistance (pZA32-*lacI-ssrA*), and the reporter module was placed on a ColE1 plasmid with ampicillin resistance (pZE12-*yemGFP-ssrA*).

## Strain construction

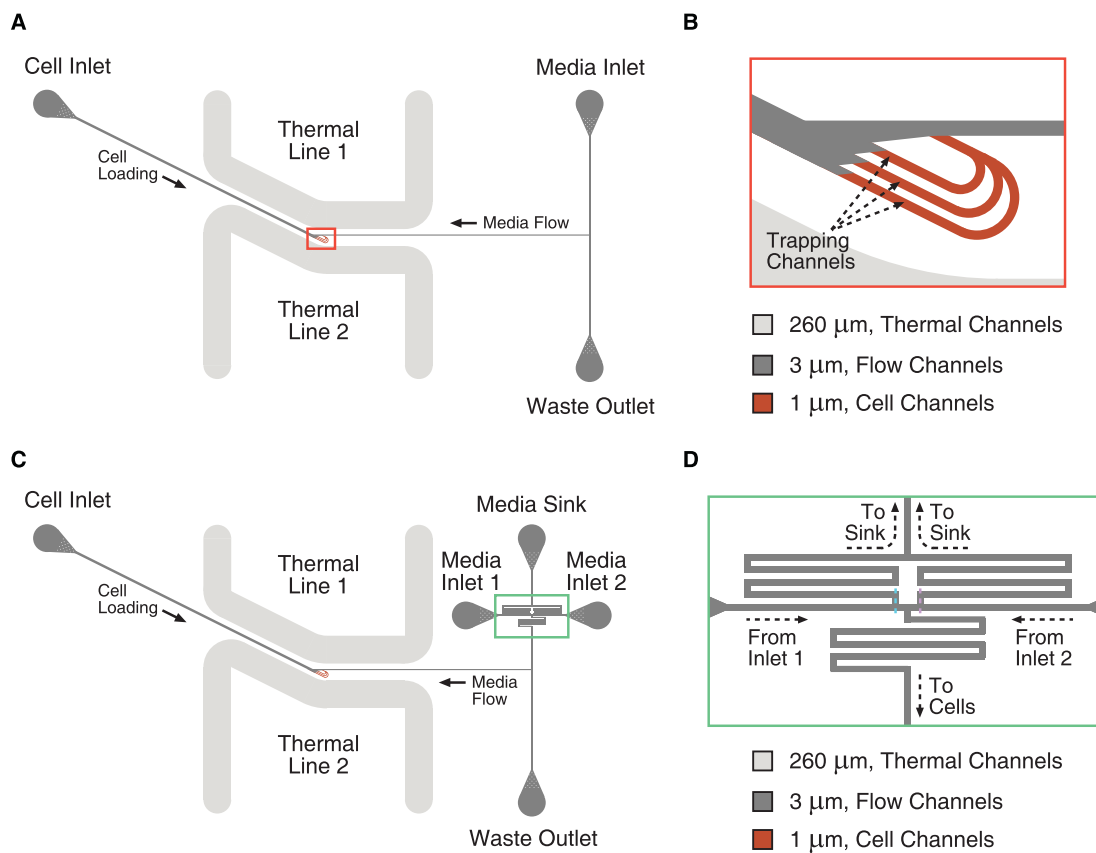
Strains of *E. coli* with deletions in *araC* (JW0063) or *lacI* (JW0336) were obtained from the Keio collection (Baba et al. 2006). Strains from this collection have single gene deletions that are linked to a kanamycin resistance marker that can be eliminated by site-specific recombination with an exogenously supplied recombinase. To construct the oscillator strain, kanamycin resistance was

eliminated from JW0063, and  $\Delta lacI$  was introduced into the resulting strain by P1vir phage transduction from JW0336. Double knockout transductants were selected for by growth on 50  $\mu\text{g}/\text{mL}$  kanamycin, and kanamycin resistance was again eliminated as above to construct strain JS006 (MG1655  $\Delta araC \Delta lacI$  Kan<sup>S</sup>). Genomic alterations were confirmed by genomic PCR (Datsenko and Wanner 2000) and sequencing. The locations of the kanamycin resistance remnants are sufficiently separated on the bacterial chromosome to prevent further recombination between deletion sites. The dual-feedback oscillator strain JS011 was constructed by transforming JS006 with pJS167 and pJS169 such that the only source of AraC and LacI was the oscillator plasmids. To construct the negative feedback oscillator strain, kanamycin resistance was eliminated from JW0336 to form strain JS002 (MG1655  $\Delta lacI$  Kan<sup>S</sup>). JS002 was then transformed with the two negative feedback oscillator plasmids described above to construct JS013.

## Microfluidics device construction

We examined cells with single-cell timelapse fluorescence microscopy using microfluidic devices designed to support growth of a monolayer of *E. coli* cells under constant nutrient flow (Supplementary Fig. 2). The use of these microfluidic devices, coupled with cell tracking and fluorescence measurement, allow us to generate fluorescence trajectories for single cells. The design of the microfluidic device used in these experiments was adapted from the Tesla microchemostat design developed in Cookson et al. (2005) for use with *Saccharomyces cerevisiae*. The original Tesla microchemostat design implemented the classic Tesla diode loop (Tesla 1920; Duffy et al. 1999; Bendib and François 2001) modified for imaging a monolayer culture of growing yeast cells. Here, modifications were made to support imaging monolayers of *E. coli*, which included lowering the cell chamber height from 4  $\mu\text{m}$  to 1  $\mu\text{m}$  to match the cylindrical diameter of K-12 MG1655 cells, lowering the delivery channel height from 12  $\mu\text{m}$  to 3  $\mu\text{m}$  to maintain equivalent flow splitting between the cell chamber and the bypass channel, and dividing the cell trapping region into three channels for simultaneous observation of isolated colonies (Supplementary Fig. 2A–B). Lastly, the width of each parallel chamber was limited to 30  $\mu\text{m}$  so as not to exceed the width/height aspect ratio of 30 for PDMS and risk structural collapse of the chamber “ceilings.”

In order to achieve long experimental runs, a critical design objective was to avoid clogging between the media port and the trapping region. Towards this end, we developed a three-port chip design in which the main channel extending from the cell port splits into a media channel and a waste channel downstream of the trapping region. The waste port receives untrapped cells during loading and superfluous media during runtime, thereby eliminating contamination of the media port. Cells were loaded into the three trapping channels of the microfluidic device by directing flow in the “forward” direction from the cell port to the waste port. Upon trapping a few cells in each region, the flow was reversed and slowed to steadily supply the cells with fresh nutrients from the media port through a combination of diffusion and advection. Cells grew exponentially to fill the channels over an experimental duration of ~4–6 hours, while images were periodically acquired in the transmitted and fluorescent channels every 2–3 min. The open walls of the trapping region allowed for cells at the periphery of the expanding colonies to be swept away by the high flow in the main channel, thus permitting continuous exponential growth long after the trapping region filled. For optimal *E. coli* growth, chip temperature was typically



**Supplementary Figure 2:** Schematics of microfluidic devices used in timelapse microscopy experiments. **A** shows the Tesla microchemostat device adapted for imaging monolayer colonies of *E. coli* over many cellular generations. Cells are loaded into the trapping channels (dark red, magnified in **B**) by directing flow from the cell inlet to the waste outlet, and then flow is reversed and slowed to provide fresh media to the cells from the media inlet during the experiment. Flow is maintained away from the media inlet at all times to prevent contamination of this reservoir. Thermal control is achieved by flowing heated water from a reciprocating bath through two high-volume thermal lines (light gray). **B** shows a magnified view of the cell trapping region (red boxed region in **A**). Cells are loaded into three parallel trapping channels for simultaneous observation of isolated colonies. The depth of these trapping channels is fabricated at precisely 1 μm to match the cylindrical diameter of K-12 *E. coli*. **C** shows a variant of the device shown in **A** with an integrated switch incorporated into the media supply line. This switch supports the selection of one of two media types and is based on laminar flow boundary shifting. **D** shows a magnified view of the switching region (green boxed region in **C**). By shifting the boundary separating the laminar flows of medium 1 and medium 2 to the channel centerline at the left (dashed blue line), flows of both media are directed to the media sink port through the shunt channels, and medium 2 is delivered to the cells. In the opposite configuration, where the laminar flow boundary is shifted to the channel centerline at the right (dashed purple line), flows of both media are directed to the media sink port through the shunt channels and medium 1 is delivered to the cells. Sustained flow of each media type to the media sink through the shunt channels prevents cross-contamination of the media reservoirs.

maintained at 37°C by flowing heated water through deep thermal channels fabricated into the device.

For on-chip induction experiments, we used a variant of the above-described device that incorporated a laminar boundary media switch into the design (Groisman et al. 2005) (Supplementary Fig. 2C). This microfabricated switch directed flow to the cells from one of two media inlet ports by shifting the boundary between the two laminar flow streams (Supplementary Fig. 2D). In these experiments, cells were loaded into the device and grown for several generations in non-inducing media without periodic image acquisition in order to minimize fluorescence exposure. Upon expanding to occupy roughly half of the field of view, the cells were induced by flipping the state of the on-chip media switch, which switched to medium with inducers in less than 1 s. We maintained constant flow from both media inlets to the media sink throughout the switching operation in order to prevent backflow contamination of the media inlets. The non-induced and induced media solutions were differentiated by labeling the inducing media with Sulforhodamine 101 red fluorescent dye. Cells grown in the absence of inducers initiated oscillations in a synchronous fashion upon the addition of inducers (Supplementary Movie 10). This initial synchrony of oscillations suggested the possibility of using flow cytometry to further characterize the oscillator.

All described devices were fabricated in the UCSD Integrated Technology Lab (ITL) and the Calit2 Nano3 facility using standard soft lithography techniques (Duffy et al. 1998; Unger et al. 2000; Whitesides et al. 2001; Sia and Whitesides 2003). Photomasks were drawn in FreeHand MX (Macromedia Inc., San Francisco, CA), printed onto transparency film by CAD/Art Services, Inc. (Output City, Poway, CA), and mounted onto borosilicate glass plates (McMaster-Carr, Los Angeles, CA). Master molds were created by first spin-coating SU-8 2000 negative photoresists (MicroChem Corp., Newton, MA) upon clean silicon wafers to appropriate depths using a Headway PWM32 programmable spinner (Headway Research Inc., Garland, TX) and then patterning using a UV contact mask aligner (HTG, San Jose, CA). Replica molds were created from master molds by mixing PDMS/Sylgard 184 (Dow Corning, Midland, MI) in a 10:1 ratio of elastomer base:curing agent, degassing in a vacuum desiccator at ~1 atm for 1 h, and curing in place over the master at 80°C for 2 h. Following removal of the PDMS monolith, chips were sectioned, bored at the fluidic ports, cleaned with HPLC-grade methanol, and permanently bonded to clean No. 1½ coverslips (Corning Inc., Corning, NY) via exposure to O<sub>2</sub> plasma at 30 W for 1 min in a 500-II Plasma Asher (Technics Plasma, Danville, CA).

### Timelapse microscopy and image analysis

All images were acquired using one of two microscopy configurations—one for brightfield imaging and another for phase contrast imaging. The brightfield setup comprised a Diaphot TMD epifluorescent inverted microscope (Nikon Instruments Inc., Tokyo, Japan) outfitted with fluorescence excitation and emission filter wheels (filter set #86006 for CFP/YFP/DsRed, Chroma Technology Corp., Rockingham, VT) and automated by a custom application written in LabVIEW (National Instruments, Austin, TX). The phase-contrast setup comprised a TE2000-U epifluorescent inverted microscope (Nikon Instruments Inc., Tokyo, Japan) outfitted with fluorescence excitation and emission filter wheels (filter set #89006 for CFP/YFP/mCherry, Chroma Technology Corp., Rockingham, VT) and a GFP filter cube (#GFP-3035B-NTE, Semrock Inc., Rochester, NY)

and automated by NIS-Elements Advanced Research software (Nikon Instruments Inc., Tokyo, Japan). Both configurations used a ProScan II XY-motorized stage with fine focus control (Prior Scientific Inc., Rockland, MA), Uniblitz VS35 high-speed shutters (Vincent Associates, Rochester, NY), an Orca-ER cooled CCD camera (Hamamatsu Photonics, Hamamatsu, Japan), and an X-Cite Series 120 fluorescent lamp (EXFO, Quebec, Canada).

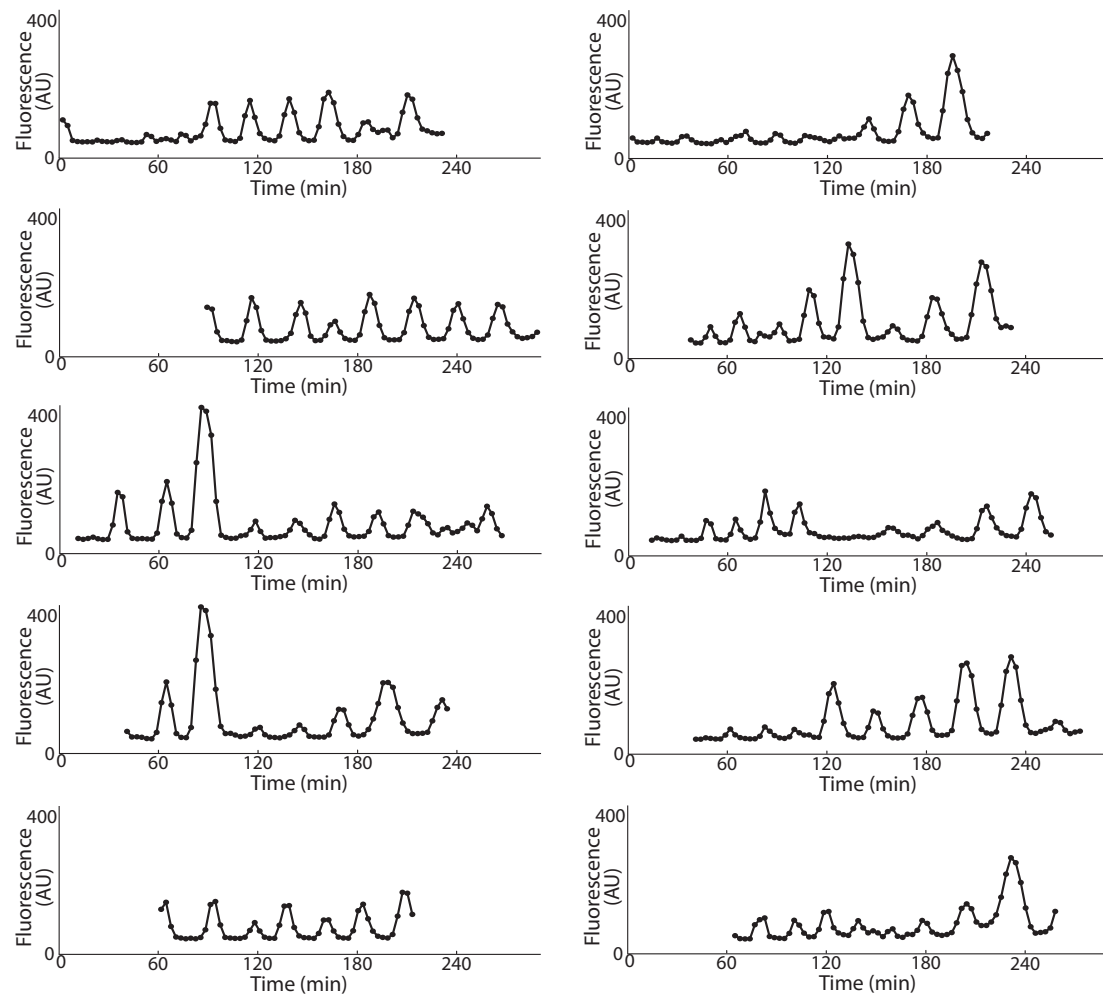
In each experiment, a microfluidic device was mounted to the stage and wetted using a solution of 0.1% Tween 20 surfactant (Sigma-Aldrich, St. Louis, MO) in the appropriate medium. Culture temperature was maintained by connecting high-volume fluidic channels fabricated into the device to a reciprocating heated/cooled water bath. Cells that had been passed from an overnight culture into inducing media approximately 3–4 h earlier were loaded into the device from the cell port by directing high flow both from the cell port and the media port to the waste port. Upon trapping a single cell in each channel, flow past the cell chamber was reversed and slowed to 1–2  $\mu\text{m}/\text{s}$  such that fresh nutrients were delivered from the media port via a combination of diffusion and advection without physically disturbing the cells.

During exponential growth of the monolayer colony, images were collected at 100x magnification in the brightfield or phase contrast and YFP or GFP fluorescence channels (for the two microscope setups described above respectively) every 2–3 min over a period of around 4–6 h. Experimental runs were often allowed to run for longer durations, but data analysis was limited to the initial period when the growth chamber had not filled. Focus was maintained during image acquisition either by manual adjustment or contrast-based autofocus algorithms. Following each imaging session, fluorescence trajectories of individual cells were extracted using the WCIF ImageJ cell analysis package (Wayne Rasband, Research Services Branch, National Institute of Mental Health, Bethesda, MD with plug-in collation and organization by the Wright Cell Imaging Facility, Toronto, ON). For each fluorescence frame, mean values of integrated fluorescence were calculated within constant circular areas inscribed within the boundaries of all tracked cells. Long-term fluorescence trajectories were subsequently constructed by manually tracking each cell throughout the experiment. Raw fluorescence trajectories were typically smooth (Supplementary Fig. 3). In cases where cell boundaries could not be resolved in the fluorescence images due to low signal, circular areas were appropriately positioned in accordance with the synchronously-collected transmitted images. The great majority of the cells showed oscillations in fluorescence (Supplementary Table 1).

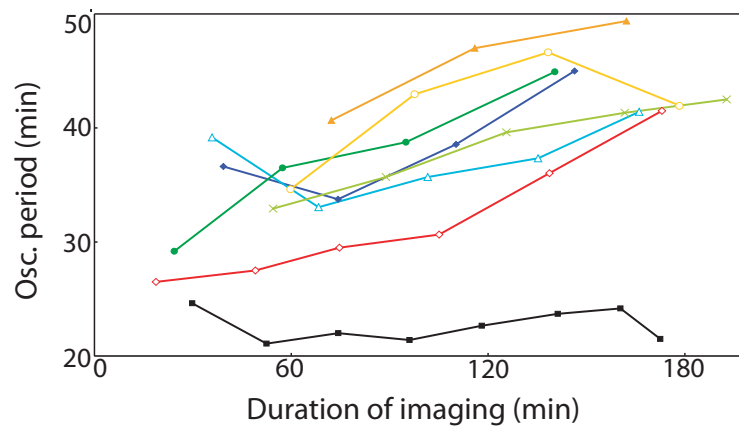
Movies of our constant-induction microscopy runs are provided as Supplementary Movies 1–9 (dual-feedback loop oscillator; JS011 in LB at 37°C (Movies 1–8) or 25°C (Movie 9)) and 11–12 (negative feedback loop oscillator; JS013 or control strain in LB at 37°C, see also Supplementary Fig. 5). Transmitted and fluorescence channels are overlaid in gray and green, respectively. Additionally, a movie capturing the dynamic induction of the dual-feedback oscillator in a partially-filled cell chamber is presented as Supplementary Movie 10 (see above). This movie demonstrates that step induction initiates synchronous oscillations within single cells of the colony.

## Flow cytometry

We initially characterized the circuit by flow cytometry of JS011 cells grown in batch cultures. An overnight culture of JS011 was diluted 1:4000 in LB (10 g/L NaCl) with 100  $\mu\text{g}/\text{mL}$  ampicillin, 50  $\mu\text{g}/\text{mL}$  kanamycin, and a range of concentrations of L-arabinose and IPTG, and grown for



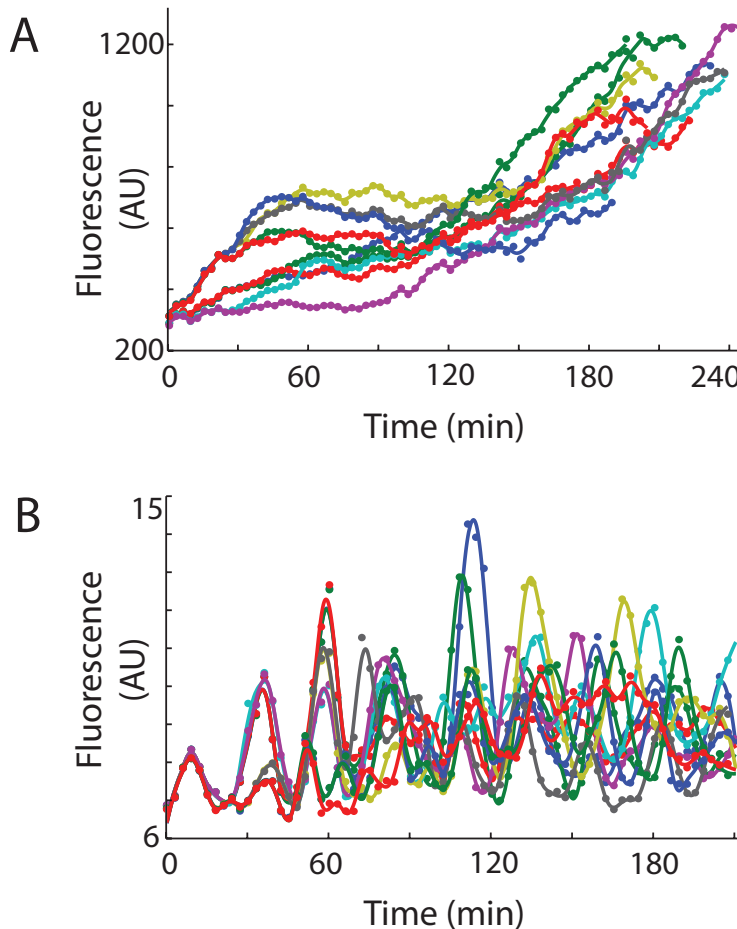
**Supplementary Figure 3:** An example of unsmoothed fluorescence trajectories. These trajectories were taken from a timelapse microscopy run at 0.7% arabinose and 0.1 mM IPTG. Each trajectory is a single cell undergoing division and oscillation. The arbitrary fluorescence units on the y-axes are equivalent.



**Supplementary Figure 4:** The effect of continued growth on oscillatory period. JS011 cells were grown in microfluidic devices for long-term single-cell imaging under inducing conditions. Each point is an average of oscillation periods from several cells at the same point in time and the same conditions (black squares, 0 mM IPTG; purple diamonds, 0.25 mM; blue triangles, 0.5 mM; green circles, 0.75 mM; green crosses, 1 mM; yellow circles, 2 mM; orange triangles, 5 mM; red diamonds, 10 mM). Data analysis was performed using custom-written MATLAB scripts.

IPTG (mM)	oscillating cells	dim cells	bright cells	dead cells
0	129	0	0	2
0.25	149	0	0	0
0.5	209	0	0	0
0.75	331	0	0	0
1	129	0	0	2
2	231	0	2	2
5	233	0	0	0
10	155	0	0	0
total	1566 (99.5%)	0	2 (0.1%)	6 (0.4%)

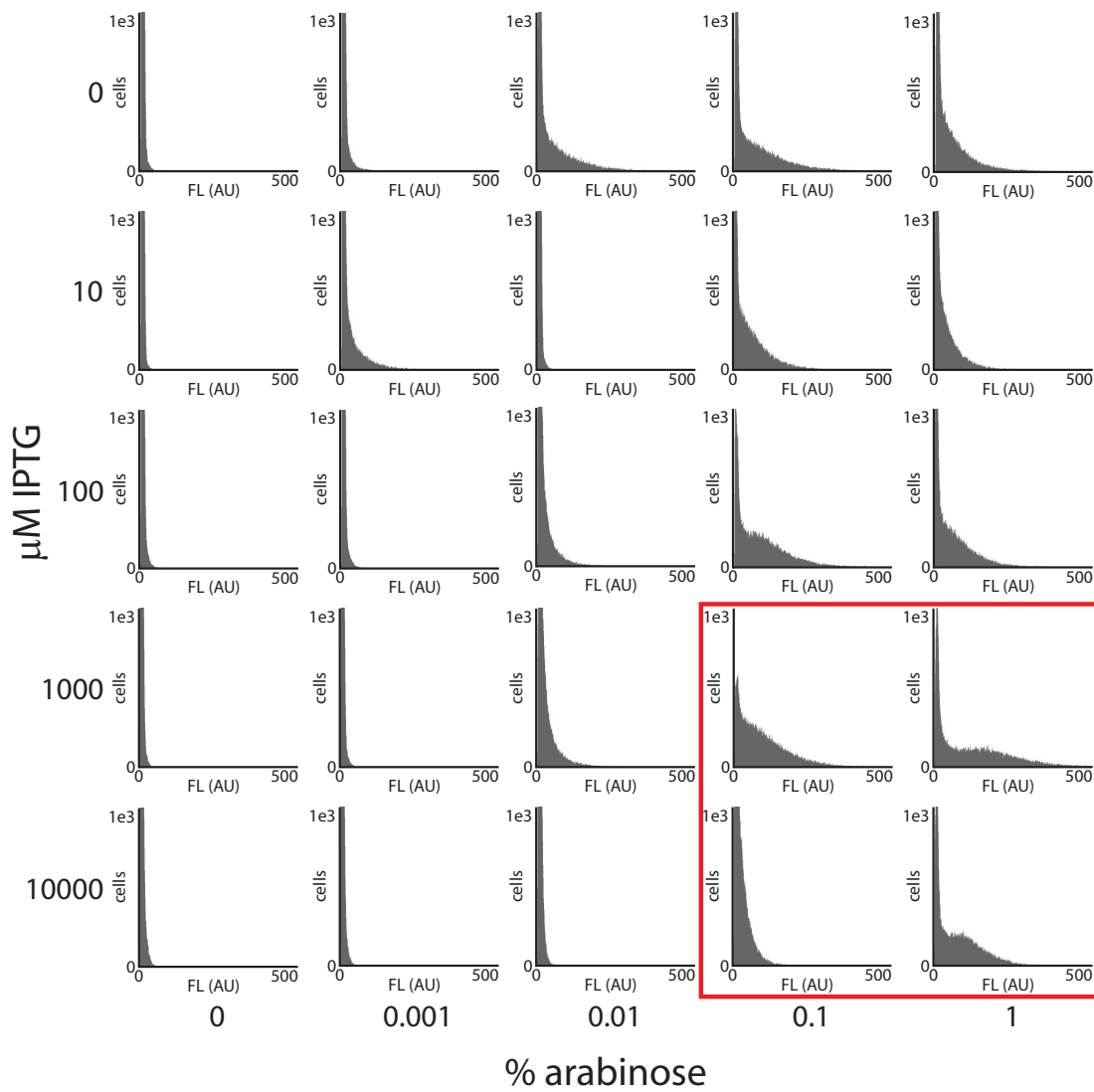
**Supplementary Table 1:** The oscillator circuit is functional in almost every cell observed with single-cell microscopy. The experiments shown in Supplementary Movies 1–8 were examined, and single cells were identified. Each cell was tracked by eye and classified into one of four groups: oscillating, never fluorescent, always fluorescent (with saturating levels of fluorescence), and dead (with abnormal morphology, usually swollen or burst, and no fluorescence).



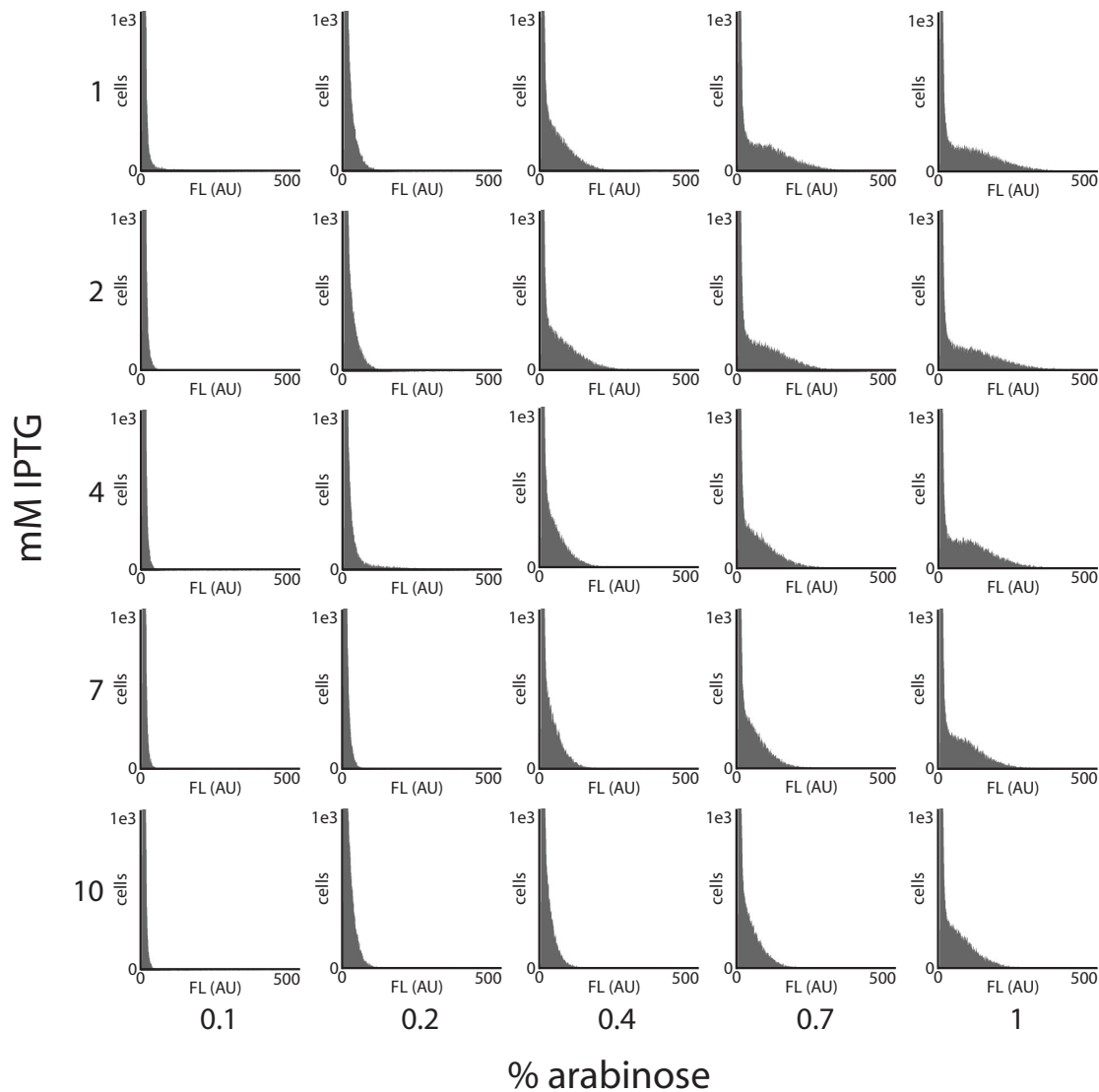
**Supplementary Figure 5:** Single-cell fluorescence trajectories for **A**, MG1655Z1/pZE12-yemGFP-ssrA cells expressing LacI constitutively and containing neither positive or negative feedback loops (induced with 2 mM IPTG), or **B**, JS013 cells containing the negative feedback oscillator (induced with 0.6 mM IPTG). Fluorescence measurements are given in arbitrary units that are consistent between the two experiments shown. Trajectories are smoothed with a Savitsky-Golay filter. Note that the cells without feedback are much brighter and do not show periodic fluorescence dynamics.

3.5 h at 37°C. Samples were washed with PBS by centrifugation, and flow cytometry analysis was performed. Our expectation was that, given a circuit that produced oscillating cellular fluorescence levels, some of the cells in an unsynchronized population would have fluorescence levels intermediate to bright and dim levels. In contrast, a monostable circuit would result in a well-defined unimodal distribution and a bistable circuit would result in a bimodal distribution with few intermediate cells. A survey of inducer space using this method revealed potentially oscillatory regions that we subsequently investigated in greater detail using flow cytometry and microscopy (Supplementary Figs. 6–7).

Additional flow cytometry was performed by one of two similar protocols. The temperature-dependence experiments followed a continuous timecourse flow cytometry protocol, in which a single culture was induced at the initial timepoint and samples were removed for flow cytometry analysis over the course of the experiment. An overnight culture of JS011 was diluted in growth

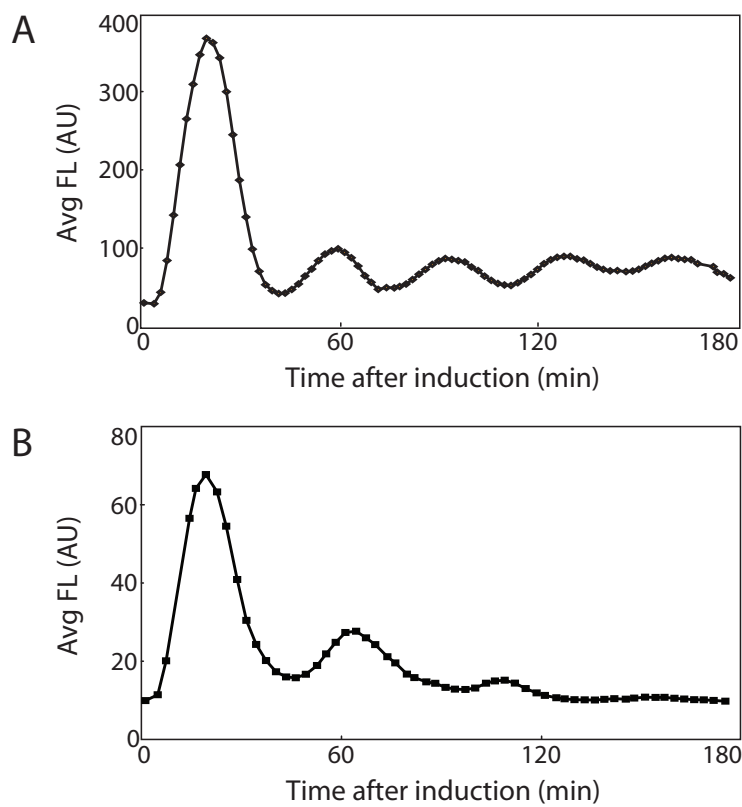


**Supplementary Figure 6:** A survey of inducer space by flow cytometry. Each subpanel is a fluorescence histogram of a flow cytometry run of JS011 grown in the presence of the indicated inducers. Fluorescence data were collected using linear mode. The x-axis of each plot is a linear scale and the y-axis of each plot is truncated at 1000 events to emphasize the shoulders in the distribution. Cells brighter than 500 AU are collected in the rightmost (brightest) bin. In each case, less than 1% of the cells fell into this bin. Distributions showing shoulders on the right side of the distribution (e.g. the area outlined in red) suggest oscillations in cellular fluorescence and were investigated more closely (see Supplementary Fig. 7).



**Supplementary Figure 7:** A closer look at shouldered fluorescence distributions at some inducer concentrations. Each subpanel is a fluorescence histogram of a flow cytometry run of JS011 grown in the presence of the indicated inducers. Fluorescence data were collected using linear mode. The x-axis of each plot is a linear scale and the y-axis of each plot is truncated at 1000 events to emphasize the shoulders in the distribution. Cells brighter than 500 AU are collected in the rightmost (brightest) bin. In each case, less than 1% of the cells fell into this bin.

medium with antibiotics and grown for 3 h at the indicated temperature with 250 rpm shaking. The OD<sub>600</sub> of the culture was ~0.01–0.02 at this point. A pre-induction sample was removed for immediate flow cytometry analysis, and inducers were added to the remaining culture to the indicated concentrations. The culture was then grown as previously and samples were removed from the culture at regular intervals for flow cytometry. Approximately every three doubling times (~70–80 min in LB) the culture was diluted 1:9 in prewarmed medium with antibiotics and inducers, and this diluted culture was used for subsequent time points. These serial dilutions kept the OD<sub>600</sub> of the culture below 0.2. The amplitude of the oscillations was initially high and decreased as the experiment continued, presumably due to desynchronization of the cells and apparent spreading of the oscillatory peaks (Supplementary Fig. 8).

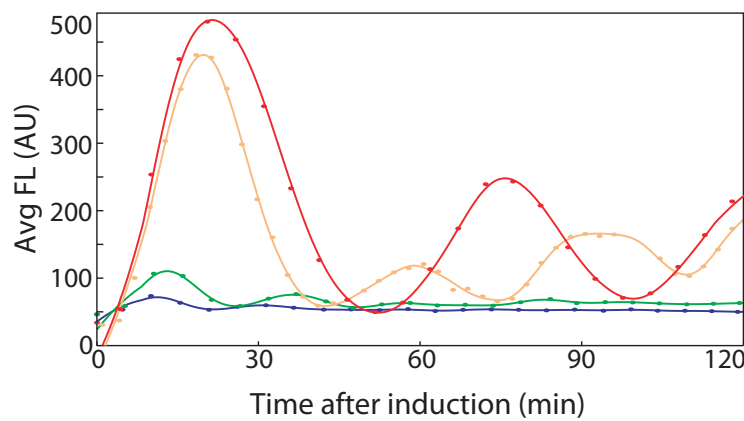


**Supplementary Figure 8:** Oscillations observed by flow cytometry. JS011 cells were grown at 37°C in either LB (**A**) or minimal A medium as in Miller (1992) with 1 µg/mL thiamine and 2 g/L glucose (**B**) plus antibiotics. Oscillations were measured by flow cytometry of samples continually harvested from growing cultures induced with 0.7% arabinose and 2 mM IPTG. Lines connecting the points are unsmoothed. In both cases, oscillations were confirmed by timelapse microscopy and shown to not decrease in amplitude over time, suggesting that the apparent ringing down of the oscillator in flow cytometry experiments is an artifact of the culture conditions or sampling method.

Inducer-dependence experiments used an aggregate timecourse flow cytometry protocol, where an uninduced culture was aliquoted onto different inducer concentrations and allowed to grow for varying lengths of time. An overnight culture of JS011 was diluted 1:100,000 in LB with antibiotics and grown at 37°C. During this growth, culture tubes containing inducers were

prewarmed. Between 2.5–4 h after initial dilution, aliquots of the growing culture were added to inducer tubes at regular intervals, resulting in a set of cultures with varying induction times. At the end of the experiment, all samples were quickly measured by flow cytometry (~3 samples/min), starting with the lowest induction duration. The induction duration was calculated as the time between addition of culture to inducer and flow cytometry measurement, and the oscillatory period was calculated as the time between the first peak and the second peak of the mean fluorescence of the culture.

This protocol allowed parallel examination of multiple inducer conditions more easily than the continuous timecourse protocol. Amplitudes and oscillation periods increased along the arabinose transect at 2 mM IPTG as arabinose increased (Supplementary Fig. 9). At low levels of arabinose, mean fluorescence was low enough that following oscillations after the second peak became difficult. However, microscopy experiments at these arabinose levels confirmed that the cells were oscillating. The values seen along the IPTG transect at 0.7% arabinose were in good agreement with the period measurements obtained from single-cell trajectories (Fig. 2a), although measurements derived from single-cell trajectories were consistently higher. This could be due to an unexplained difference in the growth environment (although doubling times were consistent across the two methods), or it could be related to the gradual increase in period seen in the microscopy experiments (Supplementary Fig. 4). Extension of the IPTG transect to IPTG levels higher than those examined by microscopy resulted in oscillations with low amplitudes and short periods, confirming the decrease in period seen in the microscopy experiments.

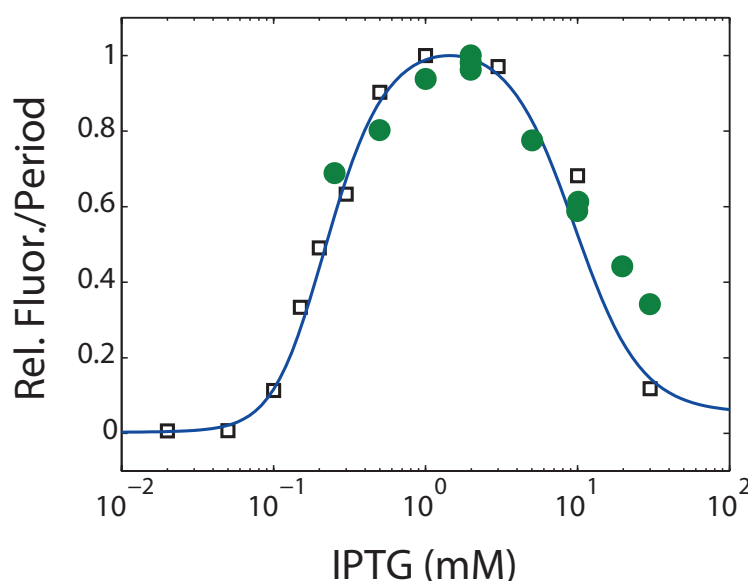


**Supplementary Figure 9:** Oscillations in mean fluorescence over time on a transect along 2 mM IPTG. Fluorescence was measured by flow cytometry of samples induced with various levels of arabinose (blue, 0.2% arabinose; green, 0.3%; orange, 0.7%; red, 2%) and 2 mM IPTG and grown for a range of durations, and smoothed by a Savitsky-Golay filter. (Flow cytometry data for the 2% arabinose sample are shown in Supplementary Figs. 14–15.)

Hybrid promoter induction curves were determined using MG1655Z1 cells (Lutz and Bujard 1997) transformed with a plasmid that contained *yemGFP-ssrA* under the control of the *plac/ara-1* hybrid promoter (essentially pJS167 without the activator module). MG1655Z1 constitutively produces LacI, which is necessary to support IPTG-mediated release of repression given the large number of *lacO* sites on multiple-copy plasmids. AraC is produced from the wildtype genomic locus. These cells have neither feedback loop from the dual-feedback oscillator. An overnight

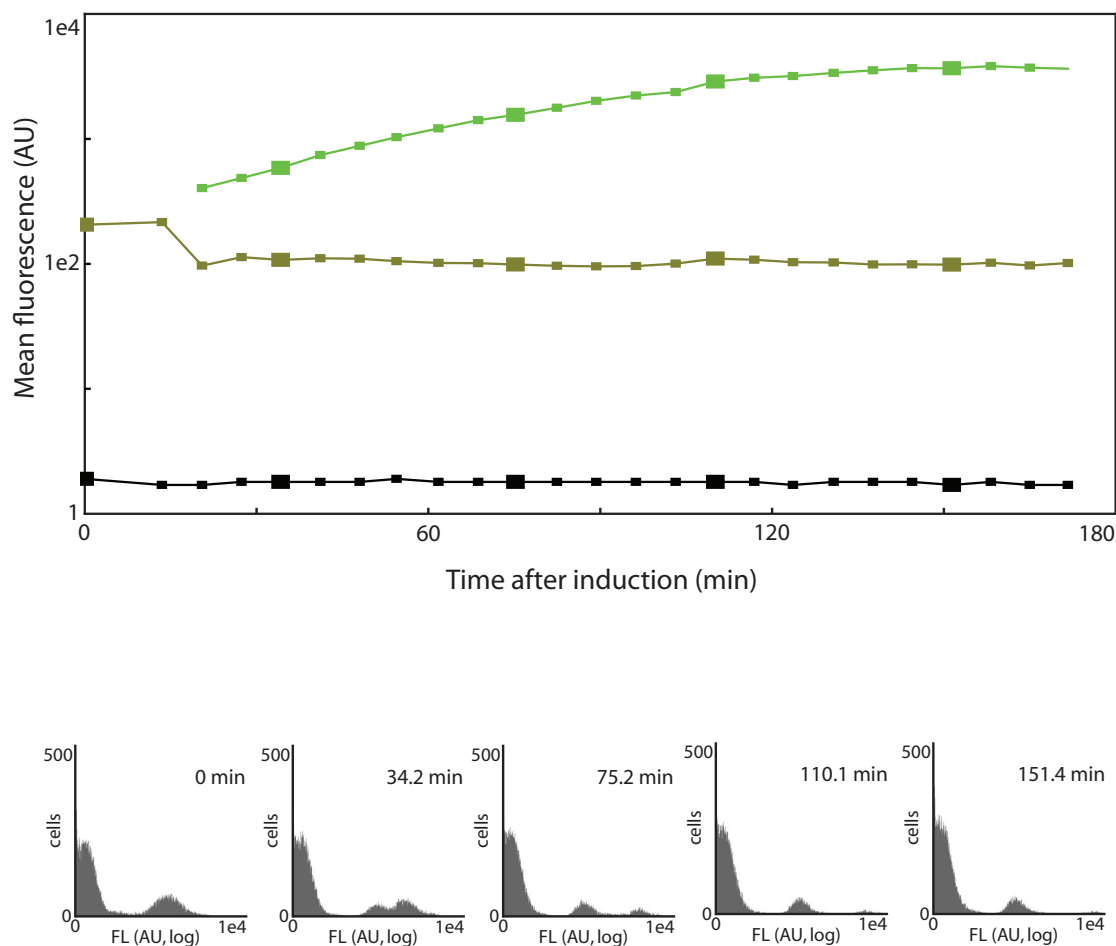
culture of these cells in LB with kanamycin was diluted 1:3000 in fresh LB with kanamycin and grown for 2 h at 37°C with shaking. The cells were then diluted 1:4 in fresh LB with kanamycin, arabinose, and varying levels of IPTG and grown for 2.5 h before being analyzed by flow cytometry.

These induction curves showed a decrease in fluorescence starting at ~2–3 mM IPTG similar to that seen in the oscillation period transect along IPTG (Supplementary Fig. 10). IPTG has been observed to interfere with AraC-arabinose binding and subsequent activation at another arabinose-inducible promoter (Lee et al. 2007). We investigated whether IPTG interfered with AraC activation of  $p_{lac/ara-1}$  using a strain with the activator but no repressor module. Arabinose induction of this system results in a runaway positive feedback loop (Supplementary Fig. 11) due to the lack of LacI repressor. This runaway induction can be prevented by IPTG addition despite the lack of LacI (Supplementary Fig. 12). We conclude that IPTG can interfere with activation of  $p_{lac/ara-1}$ , and this crosstalk in our circuit is responsible for the decreases in expression of GFP and in oscillation period that we observe.

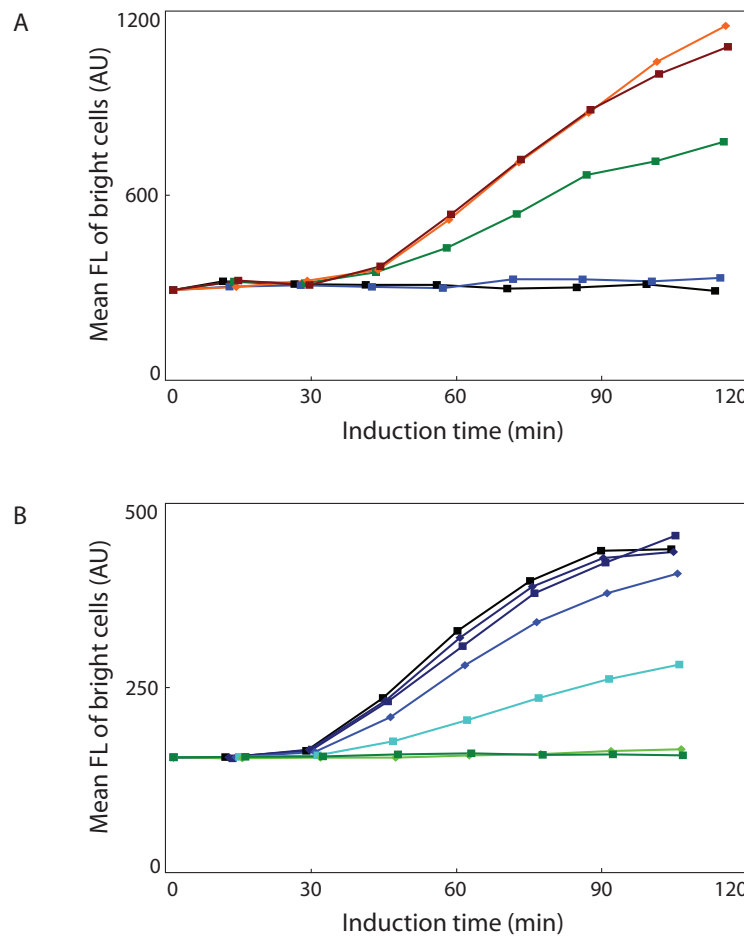


**Supplementary Figure 10:** Oscillation period dynamics mirror hybrid promoter induction. The experimental induction data from the  $p_{lac/ara-1}$  hybrid promoter in MG1655Z1 cells (with neither feedback loop, black squares) correlates well with the experimental oscillator periods determined by flow cytometry in JS011 cells (both feedback loops, green circles). Both data sets are normalized to their maximum value. The induction curve obtained from the deterministic model (blue curve) is also shown.

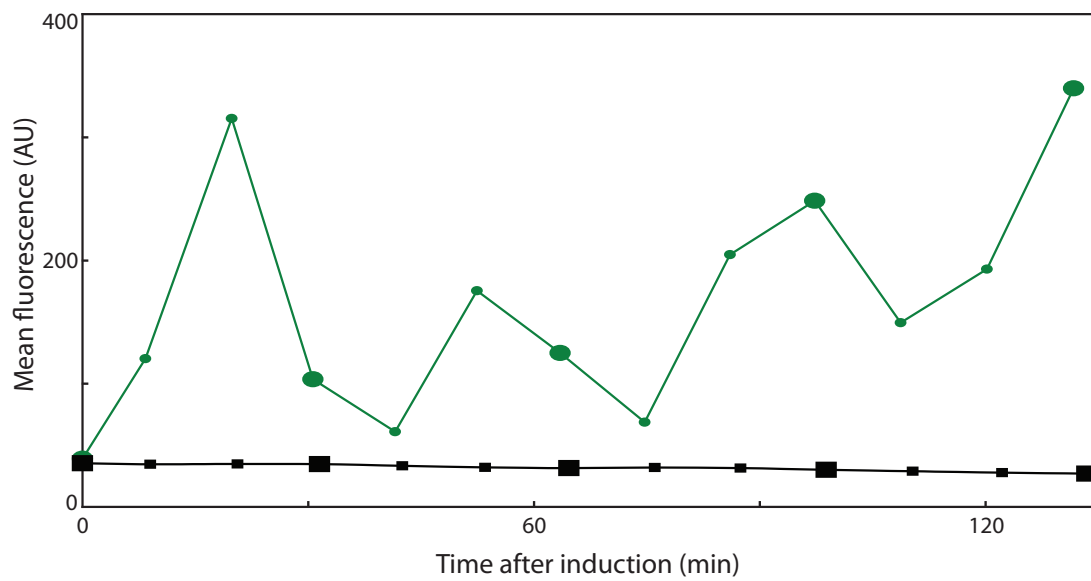
All flow cytometry analysis was carried out on a Becton-Dickinson FACScan. Unless otherwise specified, samples were read directly from the LB growth medium. Under these conditions, forward scatter histograms (at E00 voltage setting in log mode) showed two well-separated subpopulations: a low-FSC population ( $FSC < 10$ ) that was never fluorescent and a higher-FSC population that had a unimodal distribution with a mean FSC of ~70–100 and could be fluorescent. (Similar results were found with *E. coli* cells expressing GFP under a constitutive promoter, or with wildtype *E. coli* cells, except that the higher FSC population was not fluorescent with wildtype cells.) The low-FSC subpopulation was assumed to be noncellular and was removed by



**Supplementary Figure 11:** Fluorescence dynamics without the repressor module. JS006 cells ( $\Delta arac$   $\Delta lacI$ ) were transformed with pJS167 containing the activator and reporter modules. No *lacI* is present in this strain. The top panel shows timecourse flow cytometry, inducing with 0.7% arabinose and 2 mM IPTG at  $t = 0$ , on the resulting cells, which were separated into three subpopulations based on the fluorescence distributions (bottom panel). Before induction, distribution of the cells was bimodal, with a dim subpopulation (black points, left peak on the  $t = 0$  distribution) and a brighter subpopulation (olive points, right peak on the  $t = 0$  distribution). Upon induction, a third subpopulation of very bright cells separated from the bright cells (green points, rightmost on post-induction distributions). As induction continued, this subpopulation became extremely bright, increased in size, and eventually decreased in number until they were essentially eliminated from the population. The larger timepoints in the top panel correspond to the distributions in the bottom panel. (The corresponding strain without the activator module is shown in Supplementary Fig. 13.)



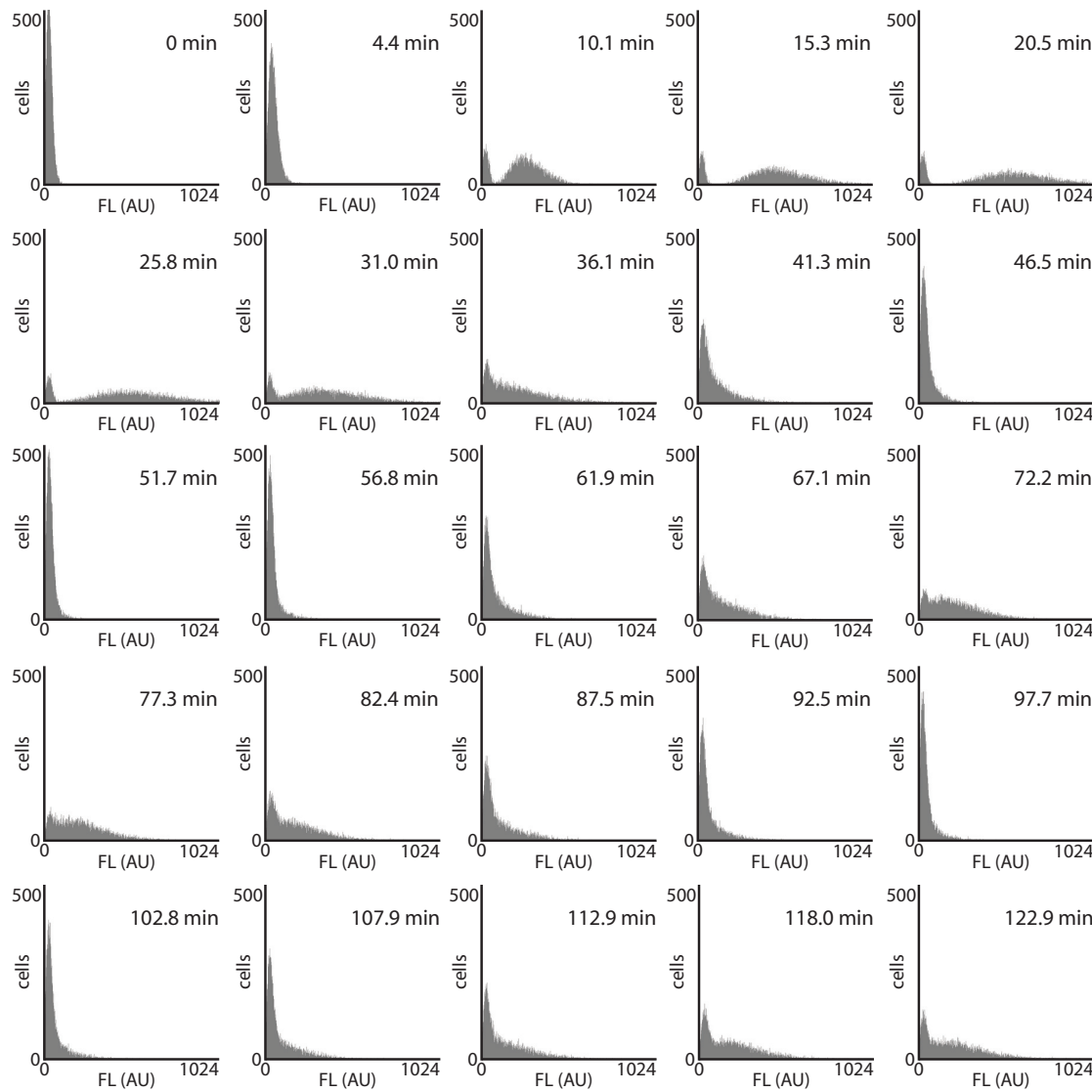
**Supplementary Figure 12:** High levels of IPTG interfere with  $p_{lac}/ara-1$  expression in the absence of LacI. JS006/pJS167 cells have a genomic *lacI* deletion and no plasmid-expressed *lacI*. Arabinose induction results in expression of additional AraC as well as GFP, giving a positive feedback loop that induces runaway GFP expression in a subset of the cells (Supplementary Fig. 11). **A**, This runaway expression can be measured by the mean fluorescence of the brightest subpopulation. Cells were grown as in Supplementary Fig. 11, induced with varying levels of arabinose (black, no arabinose; blue, 0.01%; green, 0.1%; brown, 0.3%; orange, 1%), and cellular fluorescence was measured by flow cytometry after induction. The magnitude of the effect is dependent on arabinose concentration, requires at least 0.1% arabinose, and saturates at high levels of arabinose. **B**, The addition of IPTG can interfere with this arabinose-induced runaway expression even in the absence of LacI. Cells were grown as in Supplementary Fig. 11, induced with 0.1% arabinose and varying levels of IPTG (black squares, no IPTG; dark blue diamonds, 0.1 mM; dark blue squares, 0.3 mM; blue diamonds, 1 mM; blue-green squares, 3 mM; bright green diamonds, 10 mM; dark green squares, 30 mM), and cellular fluorescence was measured by flow cytometry after induction. IPTG interference with runaway activation required 1–3 mM IPTG and was total at 10 mM IPTG.



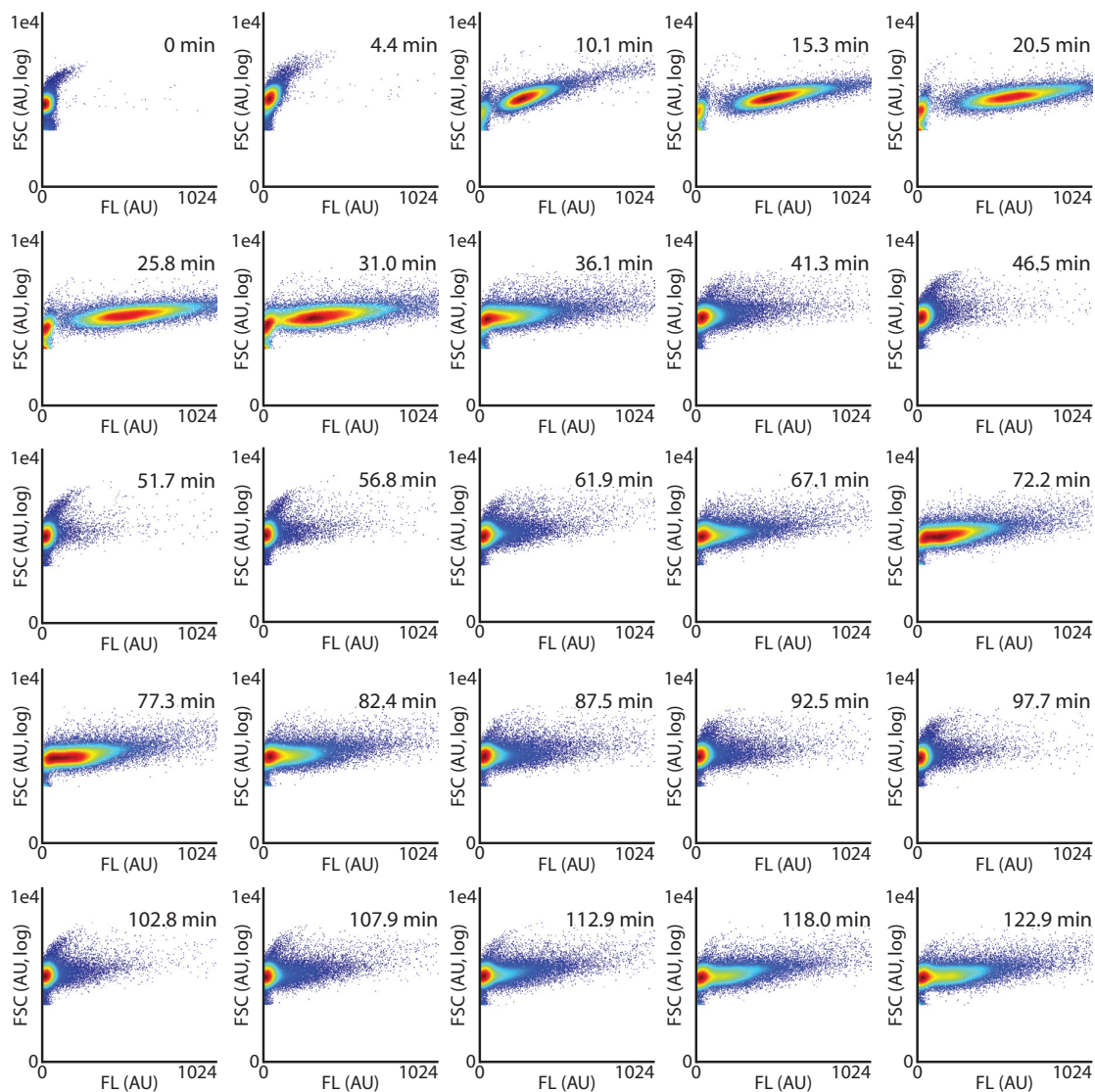
**Supplementary Figure 13:** Fluorescence dynamics without the activator module. JS006 cells ( $\Delta araC \Delta lacI$ ) were transformed with pJS169 containing the repressor module and pZE24-yemGFP-LAA, a pJS169-derived plasmid with the reporter module but without the activator module. No *araC* is present in this strain. The top panel shows timecourse flow cytometry, inducing with 0.7% arabinose and 2 mM IPTG at  $t = 0$ , on the resulting cells (black, square points), and on JS011 cells with both oscillator components (green, circular points) for scale. The bottom panel shows fluorescence distributions from JS011 cells with both components (top row) and cells with repressor only (bottom row). The larger timepoints in the top panel correspond to the distributions in the bottom panel.

setting the event threshold on the flow cytometer at  $FSC = 20$ . Fluorescent detector voltages (and gains if reading in linear mode) were adjusted to the dynamic range appropriate for a particular experiment. For the oscillator characterization experiments, the settings were linear mode, voltage 825–975, gain 8.00–8.25. Any samples that were compared to each other were run under identical settings. For each time point, 25,000–100,000 events were collected at low flow rate.

In our single-cell microscopy experiments, the vast majority of cells oscillated (see Supplementary Table 1). In contrast, in the flow cytometry experiments, there was a subpopulation of cells of slightly smaller forward scatter that did not fluoresce (Supplementary Figs. 14–15). We assume that this subpopulation was essentially static, as the proportion of cells it contained could be seen to be constant over time if the oscillating subpopulation was sufficiently separated. The proportion of this subpopulation was larger at lower inducer concentrations. Inclusion of these cells in flow cytometry data analysis decreases the mean cellular fluorescence proportional to their frequency, but it does not affect the timing of oscillatory peaks (and therefore period determination). In the microscopy experiments, the cells were grown in the presence of inducer before and during loading into the microfluidic device. In contrast, the flow cytometry experiments observed the cells immediately after induction. The cell strain used here has the arabinose transporter genes under native regulation. Since these genes are positively regulated by AraC-arabinose, this gives a positive feedback loop that results in bimodal populations at some arabinose concentrations (Siegele and Hu 1997). Due to stochastics, some cells will have low initial levels of arabinose transporters and respond poorly to arabinose, while others will have higher initial levels of arabinose transporters and respond well to arabinose. We suggest that the longer exposure to arabinose before observation in the single-cell microscopy experiments results in autoinduction of the arabinose transporters in the great majority of the cells. In contrast, in the flow cytometry experiments at lower arabinose concentrations, a subpopulation of cells does not autoinduce sufficient arabinose transporter expression to respond to arabinose.



**Supplementary Figure 14:** Fluorescence distributions from timecourse flow cytometry analysis of the 2% arabinose and 2 mM IPTG sample. For each timepoint collected in this experiment, a histogram of fluorescence values is shown here. (The mean fluorescence value over time is shown in Supplementary Fig. 9.) Fluorescence data were collected in linear mode. Note that the majority of the population oscillates, but there is a small subpopulation that does not fluoresce.



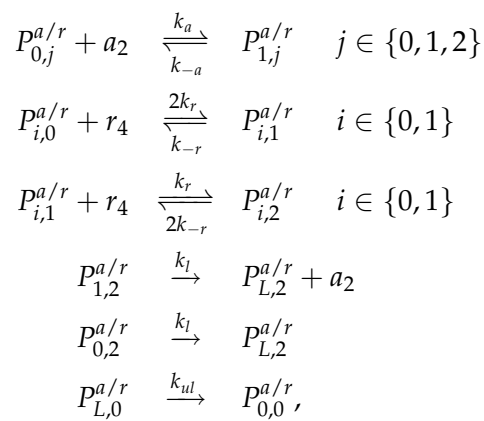
**Supplementary Figure 15:** Forward scatter versus fluorescence distributions from timecourse flow cytometry analysis of the 2% arabinose and 2 mM IPTG sample. For each timepoint collected in this experiment, a density plot of forward scatter versus fluorescence is shown. (The mean fluorescence value over time is shown in Supplementary Fig. 9.) Fluorescence data were collected in linear mode, while forward scatter data were collected in logarithmic mode and low forward scatter noise was removed as described in Supplementary Methods.

## Modeling

### The underlying reactions of the stochastic and deterministic models

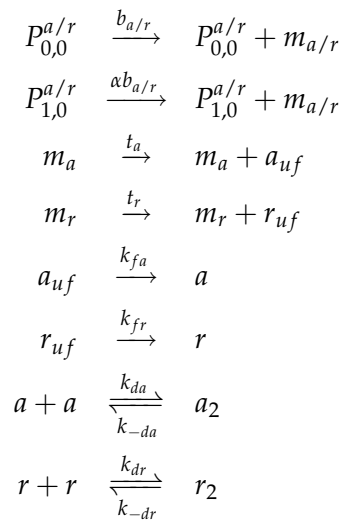
Because of the dynamical nature of the oscillators we have constructed, we have used mathematical modeling to both gain insight into and make predictions about their behavior. Our models are based on the following chemical reactions.

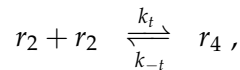
The dynamics of the promoters are given by the following set of reactions:



where  $P_{i,j}^{a/r}$  represent the states of promoters on the (a)ctivator/(r)epressor plasmids with  $i \in \{0, 1\}$  AraC dimers ( $a_2$ ) bound and  $j \in \{0, 1, 2\}$  LacI tetramers ( $r_4$ ) bound. The states  $P_{L,j}^{a/r}$  represent looped forms of the DNA, on which AraC is forbidden to bind. Once two LacI tetramers are bound, the plasmid may loop, forming a tight complex which must be unfolded to release repression. We did explore the inclusion of reverse reactions for the looping. However, when we assumed that the reverse reaction rates were small compared to the forward rates, the behavior of the system was unchanged.

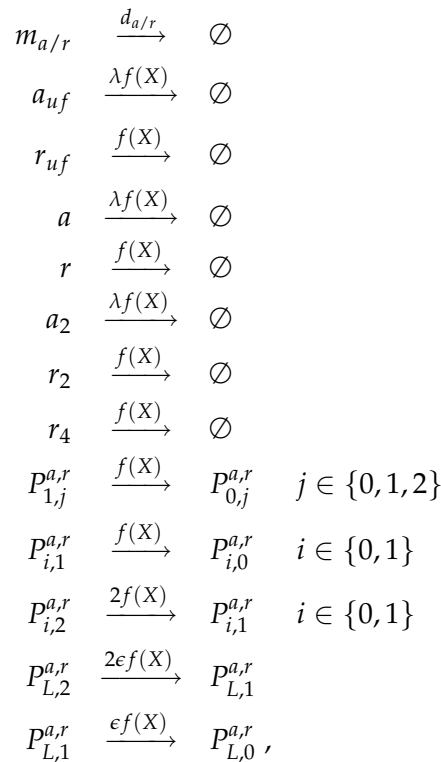
The next set of reactions govern the transcription, translation, protein folding, and multimerization of each gene/protein:





where  $m_{a/r}$  represents the number of activator/repressor transcripts;  $a_{uf}$  and  $r_{uf}$  are the unfolded monomeric versions of the activator and repressor;  $a$  and  $r$  are the folded monomeric versions of activator and repressor;  $a_2$  and  $r_2$  are the dimeric versions of activator and repressor; and  $r_4$  is the tetrameric version of repressor.

Finally, the mRNA transcripts decay exponentially, and all tagged forms of protein decay enzymatically according to the following set of reactions:



where

$$f(X) = \frac{\gamma}{c_e + X}$$

and  $X$  is the total number of *ssrA* tags in the system (one for each monomeric version, two for dimers, and four for tetramers, including proteins bound to operator sites).

The parameters used for the simulations were:  $b_a = b_r = 0.36 \text{ min}^{-1}$ ,  $\alpha = 20$ ,  $k_{-a} = k_{-r} = 1.8 \text{ min}^{-1}$ ,  $t_a = t_r = 90 \text{ min}^{-1}$ ,  $d_a = d_r = 0.54 \text{ min}^{-1}$ ,  $k_{fa} = k_{fr} = 0.9 \text{ min}^{-1}$ ,  $k_{da} = k_{dr} = k_t = 0.018 \text{ min}^{-1} \text{ molecules}^{-1}$ ,  $k_{-da} = k_{-dr} = k_{-t} = 0.00018 \text{ min}^{-1}$ ,  $k_l = 0.36 \text{ min}^{-1}$ ,  $k_{ul} = 0.18 \text{ min}^{-1}$ ,  $\gamma = 1080 \text{ molecules/min}$ ,  $c_e = 0.1 \text{ molecules}$ ,  $\lambda = 2.5$ , and  $\epsilon = 0.2$ . The total number of activator plasmids was estimated to be  $N_a = 50$  and the number of repressor plasmids to be  $N_r = 25$ . The forward binding rates of the activator dimer and repressor tetramer to the operator sites are

dependent upon the concentrations of arabinose and IPTG. Specifically, we defined:

$$k_r = k_{-r} \left( \left( C_r^{\max} - C_r^{\min} \right) \cdot \frac{1}{1 + \left( \frac{[IPTG]}{k_{r1}} \right)^{b_1}} + C_r^{\min} \right), \quad (1)$$

where  $C_r^{\max} = 0.2 \text{ molecules}^{-1}$  and  $C_r^{\min} = 0.01 \text{ molecules}^{-1}$  are the maximum and minimum affinities of LacI tetramers to the binding site,  $[IPTG]$  is the IPTG concentration (in mM),  $k_{r1} = 0.035 \text{ mM}$ , and  $b_1 = 2$ . Similarly, we defined:

$$k_a = k_{-a} \left( \left( C_a^{\max} - C_a^{\min} \right) \cdot \frac{[ara]^{c_1}}{k_{a1}^{c_1} + [ara]^{c_1}} \cdot \frac{1}{1 + \left( \frac{[IPTG]}{k_{r2}} \right)^{b_2}} + C_a^{\min} \right), \quad (2)$$

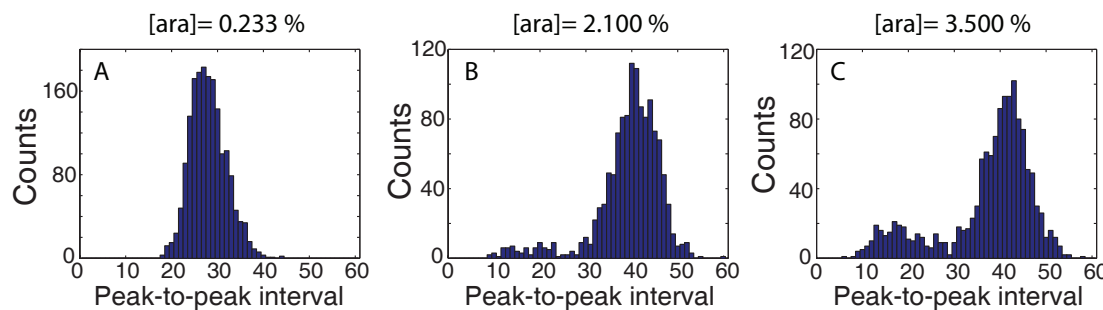
where  $C_a^{\max} = 1 \text{ molecules}^{-1}$  and  $C_a^{\min} = 0 \text{ molecules}^{-1}$  are the maximum and minimum affinities of AraC dimers to the binding sites,  $[ara]$  is the concentration of arabinose (in % w/v),  $k_{a1} = 2.5\%$ ,  $k_{r2} = 1.8 \text{ mM}$ ,  $c_1 = 2$ , and  $b_2 = 2$ .

The stochastic simulations were performed using Gillespie's algorithm (Gillespie 1977) using custom written software in the C programming language, while deterministic simulations on the corresponding mass-action ODEs were performed using custom written software in MATLAB.

### Theoretical predictions of oscillation period versus arabinose concentration

These computational models can also be used to calculate the oscillation period as a function of arabinose concentration. However, interpretation of the model is complicated by the existence of two bistable states. The first of these states corresponds to the large amplitude (and hence long period) oscillations that are the hallmark of the oscillator. In addition to this state, there is a second state, which for low arabinose levels is a stable limit cycle with very low amplitude and short period. The basin of attraction for this limit cycle appears to be very small, so that it is rarely (if ever) seen stochastically. The intrinsic noise of the system ensures that (1) the probability of reaching this state is small and (2) when the system does reside in this state, it does not remain there for long. This is illustrated in Supplementary Fig. 16A, which shows the peak-to-peak interval distribution for the stochastic model at 2 mM IPTG and 0.233% arabinose. The distribution is unimodal, with a mean that is equal to the period of the large amplitude oscillations observed in the deterministic model. As the arabinose concentration increases, the small amplitude limit cycle goes through a Hopf bifurcation near  $[ara] = 1.83\%$ , above which the limit cycle becomes a stable fixed point. Stochastically, however, the intrinsic noise creates small-amplitude noise-induced oscillations whenever the system is near the fixed point. The system will most often reside in the large amplitude oscillation state, but will occasionally jump to the noise-induced oscillations for brief periods of time. For example, Supplementary Fig. 17 shows a typical trajectory obtained from stochastic simulations. The basin of attraction of these noise-induced oscillations becomes larger as the arabinose concentration is increased. This can be seen in Supplementary Fig. 16B–C, which show the peak-to-peak interval distributions for  $[ara] = 2.1\%$  and  $[ara] = 3.5\%$ , respectively. Just above the Hopf point (Supplementary Fig. 16B),

the system resides mainly in the large amplitude state, with just a few incursions into the noise-induced oscillatory state. For higher arabinose concentrations, however, the amount of time spent in the small amplitude state increases due to the enlargement of the basin of attraction (Supplementary Fig. 16C).

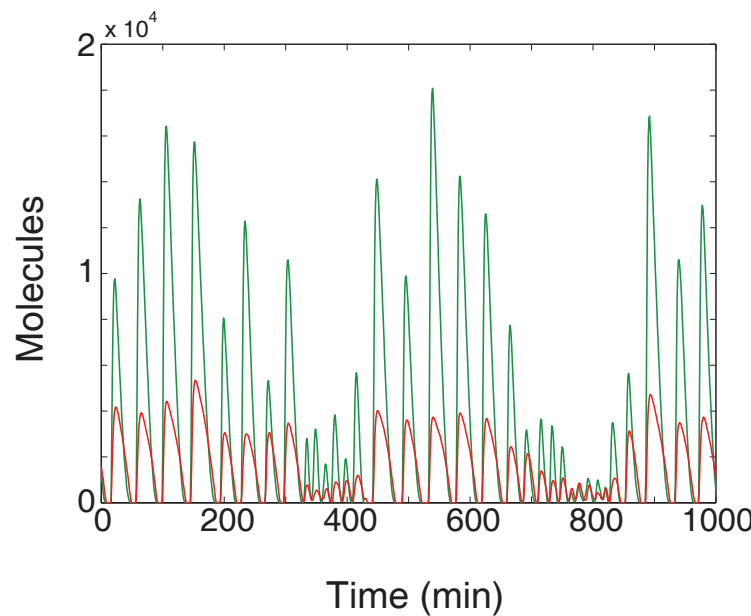


**Supplementary Figure 16:** Histograms of peak-to-peak intervals for the stochastic model of the oscillator. **A**, At low arabinose the distribution of peak-to-peak intervals is unimodal, with a mean equal to the deterministic period. **B**, When the arabinose concentration increases above 1.83%, bistable oscillations arise. The system stochastically switches between the two forms of oscillation, giving rise to a bimodal peak-to-peak interval distribution. **C**, As the arabinose concentration increases further, the amount of time spent in the low amplitude oscillation state increases.

To obtain the stochastic period, we must make a decision as to what statistic of the peak-to-peak distribution to measure. If we were to blindly calculate the mean of the distribution, the period would appear to decrease for increasing arabinose levels, since the time spent in the low amplitude (and hence low period) state becomes ever larger. This can be seen in Supplementary Fig. 18, which shows the period of the oscillator as a function of arabinose concentration at 2 mM IPTG. The experimentally measured values of the period are shown by green and red points, while the values predicted by the deterministic model (in the large-amplitude oscillatory state) are shown by the blue curve. Also shown are three possible measures of the period taken from the stochastic simulations. The gray triangles represent the value of the period obtained from taking the absolute mean of the peak-to-peak distribution. As expected, that measure of the period decreases at high arabinose levels.

Another possible way to measure the mean period of the stochastic simulations is to ignore the low amplitude oscillations, and concentrate instead on the upper half of the peak-to-peak distribution. Roughly speaking, this can be done by ignoring all intervals that are less than 30 min (provided the arabinose concentration is greater than 1.0%). Such a measure is roughly tantamount to measuring the mode of the whole distribution, provided more time is spent in the large amplitude state. The gray squares in Supplementary Fig. 18 show this measure of the period, and they match well with the deterministic period.

It is interesting to point out that many of the experimentally measured values of the period in Supplementary Fig. 18 were obtained through timelapse flow cytometry. Because the amplitude of the long period state is so much higher than the short period state, it is unlikely that small amplitude oscillations would be detectable even if they were occurring. Therefore, one final measure of the period may also be relevant. Time spent in the small amplitude region could



**Supplementary Figure 17:** An example of bistable oscillations in the stochastic model at high arabinose. Here  $[ara] = 3.5\%$  and  $[IPTG] = 2\text{ mM}$ . The green curve is the number of free AraC dimers, while the red curve is the number of free LacI tetramers.

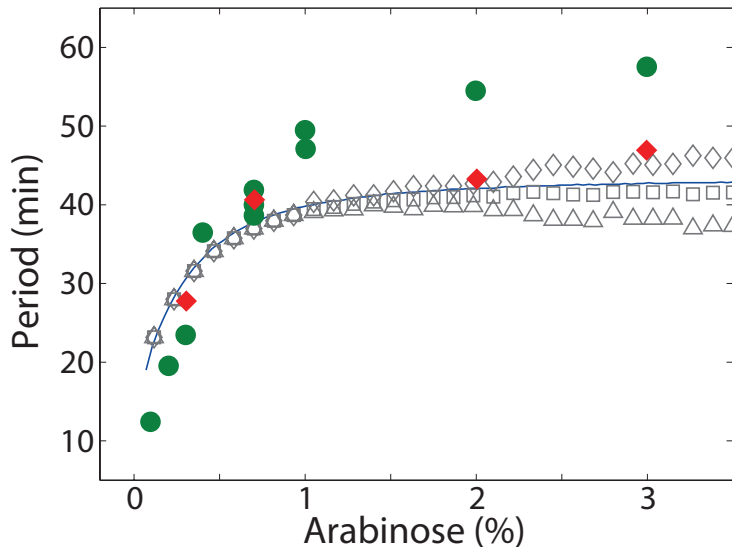
be considered as additional time between the two large amplitude peaks which border it. If the low amplitude oscillations are ignored (i.e. not considered as peaks at all) and the resulting gaps added to the interval between the bordering peaks, the peak-to-peak distribution will be skewed towards the long period regime. The gray diamonds in Supplementary Fig. 18 show the resulting period of the stochastic simulations measured in this way.

As of yet, we have no experimental evidence that bistable oscillations occur in the oscillator. As mentioned above, low amplitude oscillations will probably be washed out of any measure obtained through flow cytometry. Additionally, our single cell measurements obtained through microscopy at high arabinose concentrations have not revealed any cells oscillating with a low period. However, due to the low number of cells present in the imaging chamber, combined with the limited amount of time that reliable images can be taken, it may be that we have not been fortunate enough to observe such oscillations yet. It is also possible that the stochastic model is either in the wrong parameter regime or is missing an important component of the network that would preclude bistability. We plan on investigating this in future studies.

### Theoretical predictions of oscillation period versus temperature

It is well known that the cell cycle time of *E. coli* depends on temperature according to the formula

$$\tau_{cc}(T) = \tau_{ref} \exp \left\{ \Theta_{cc} \left[ 1/T - 1/T_{ref} \right] \right\}, \quad (3)$$



**Supplementary Figure 18:** The period of oscillation as a function of arabinose concentration (at 2 mM IPTG). Shown are the experimentally measured periods obtained through timelapse flow cytometry (green circles) or single-cell microscopy (red diamonds), the periods predicted by the deterministic model (blue curve), and the periods predicted by the stochastic model, measured in three ways (gray symbols). The triangles are the raw mean of the peak-to-peak distributions; the squares are the mean of the right hand side of the distributions (roughly the mode); and the diamonds are the mean of peak-to-peak distributions in which only large amplitude peaks are considered (so that small amplitude oscillations are considered part of one long period oscillation).

where  $\tau_{cc}(T)$  is the cell cycle time as a function of temperature  $T$ , in Kelvin;  $\tau_{ref}$  is a reference time at the reference temperature  $T_{ref}$ ; and  $\Theta_{cc}$  is a constant. We measured the doubling times of the JS011 strain at various temperatures and calculated  $\Theta_{cc} \approx 8300$  K.

In order to predict the frequency of oscillations at various temperatures in the model, each rate constant must be multiplied by a similar Arrhenius constant, such that

$$k_i = k_{ref} \exp \left\{ -\Theta_i [1/T - 1/T_{ref}] \right\}, \quad (4)$$

where  $k_i$  is the  $i^{\text{th}}$  rate constant in the model, and  $\Theta_i$  is the constant associated with that reaction. Each reaction will have a different value for  $\Theta_i$ , and these constants are, in general, not known. If, however, we assume that  $\Theta_i \approx \Theta_{cc} \forall i$ , then calculating the temperature dependence of the model is equivalent to scaling time by the Arrhenius factor, since all affected model constants have an inverse time as part of their units. Therefore, we can determine the period of the model from the equation

$$P(T) = P_{ref} \exp \left\{ \Theta_{cc} [1/T - 1/T_{ref}] \right\}, \quad (5)$$

where  $P$  is the period and  $P_{ref}$  is the period at  $T = T_{ref}$ . Fig. 2c shows the model's prediction of the period based on the reference temperature  $T_{ref} = 30^\circ\text{C}$  and reference period  $P_{ref} = 69$  min.

## Negative feedback-only oscillations

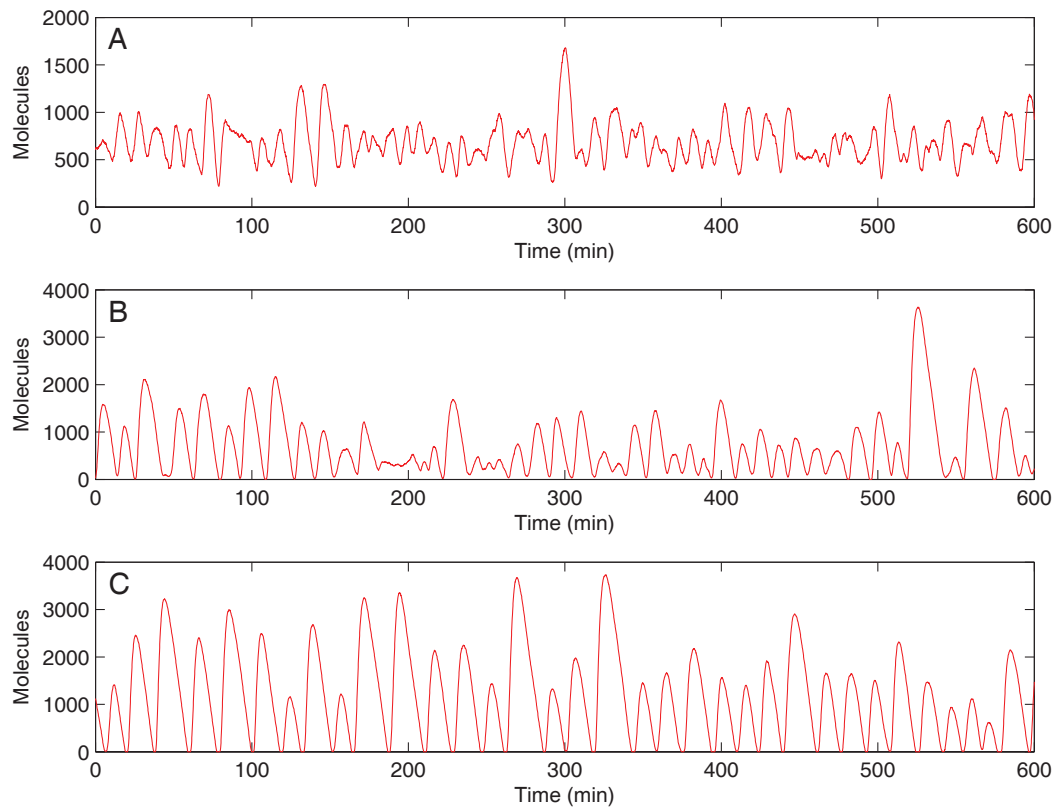
Even without the positive feedback loop, the model of our circuit exhibits oscillations. However, their properties may depend on the specific way in which the negative feedback-only system is constructed. In particular, we find that the forward rate of DNA looping reaction  $k_\ell$  plays an important role. We illustrate this with three different variants of a negative feedback-only system, with different values of  $k_\ell$ . For all variants, we set the number of plasmids that produce AraC to zero (i.e.  $N_a = 0$ ), ensuring that AraC is not produced and that repressor does not interact with DNAs residing on those plasmids. We also increase the basal transcription rate of LacI by setting  $b_r = 10 \text{ min}^{-1}$ . Other parameters coincide with the listed values for the dual-feedback model.

Our first example of a negative feedback-only system is characterized by a lack of DNA looping ( $k_\ell = 0$ ) and roughly corresponds to our experimental negative feedback-only system. A typical time series obtained from this stochastic model is shown in Supplementary Fig. 19A. As seen from the Figure, the amplitude of these oscillations is relatively small, and the LacI concentration does not go all the way down to zero in the troughs of oscillations. The oscillations are noticeably less regular than those in the original dual-feedback model. In fact, for  $[\text{IPTG}] > 0.2 \text{ mM}$ , the oscillations decay in the deterministic version of the model and are persistent only in stochastic simulations. However, for very small values of  $[\text{IPTG}] < 0.2 \text{ mM}$ , large-amplitude oscillations are observed (not shown). We examined the system for a number of values of  $[\text{IPTG}]$  up to  $1 \text{ mM}$  and found that the characteristic period of oscillations was remarkably less tunable than in the dual-feedback oscillator model (Supplementary Fig. 20). These features are consistent with our experimental findings for the  $p_{\text{LlacO-1}}$  promoter that lacks DNA looping and is transcribed at a high level.

In our second example of a negative feedback-only system, DNA looping is present with the same rate,  $k_\ell$ , as in the original dual-feedback model. In this case, we observe larger and more regular LacI oscillations for a wide range of  $[\text{IPTG}]$  in which LacI goes to zero in the troughs of oscillations (Supplementary Fig. 19B). However, the period of oscillations is still not sensitive to varying  $[\text{IPTG}]$  concentration (Supplementary Fig. 20).

Finally, we tested the model with  $k_\ell$  that is 1000 times larger than our nominal value for the dual-feedback model. In this case, large-amplitude and regular LacI oscillations are again observed for a wide range of  $[\text{IPTG}]$  (Supplementary Fig. 19C). The period of these oscillations is somewhat longer than for original  $k_\ell$  and remains only weakly tunable with respect to varying  $[\text{IPTG}]$  (Supplementary Fig. 20).

We conclude from these simulations that negative feedback-only systems may lead to oscillations. However, the properties of these oscillations vary depending on system parameters. The negative feedback-only system oscillates only weakly in the experiments, in agreement with the model without DNA looping. The addition of a positive feedback loop in this case leads to an increased robustness of such oscillations. However, due to other possible differences between the  $p_{\text{lac/ara-1}}$  promoter in the experimental dual-feedback system and the  $p_{\text{LlacO-1}}$  promoter in the experimental negative feedback-only system, further experimental work is needed to calibrate the model and test these predictions. Furthermore, it appears that for other experimental implementations, negative feedback-only systems may by themselves generate large-amplitude robust oscillations. A quest for such simplified designs is currently underway.



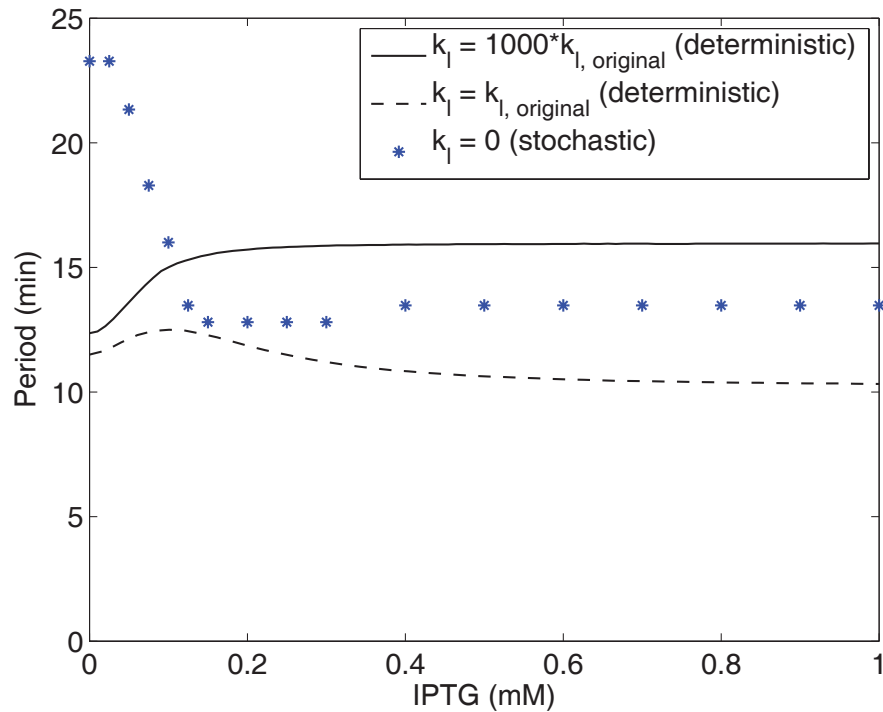
**Supplementary Figure 19:** Characteristic time series of free LacI tetramer obtained from negative feedback-only stochastic models. Here  $b_r = 10 \text{ min}^{-1}$  and  $[\text{IPTG}] = 2.0 \text{ mM}$ . Negative feedback-only systems were tested for three different values of the DNA looping rate constant  $k_\ell$ : **A**,  $k_\ell = 0$ , i.e. when DNA looping is not present; **B**,  $k_\ell = 0.36 \text{ min}^{-1}$ , the value used in the dual-feedback model; **C**,  $k_\ell = 360 \text{ min}^{-1}$ .

## On the robustness of oscillations

The formulation of design principles that lead to the creation of robust gene circuits is a major goal in synthetic biology. Robust circuits are insensitive to the precise tuning of system parameters and thus can cope with the natural variability found *in vivo* (Elowitz et al. 2002). The model of the bacterial oscillator proposed here suggests that delay in negative feedback may be key in explaining the experimentally observed robustness of oscillations. Such delay may arise from a variety of intermediate steps, e.g. multimerization, folding, and maturation, which combine into a net delay that promotes oscillatory behavior. The sharpness of a distributed delay may also be relevant in this regard (Rateitschak and Wolkenhauer 2007).

The relationship between feedback delay and robustness can be simply traced in the case of certain delayed negative feedback gene circuits. Such circuits include the negative feedback oscillator described here with constitutive activator and no positive feedback. A minimal model in this case is the first-order delay-differential equation

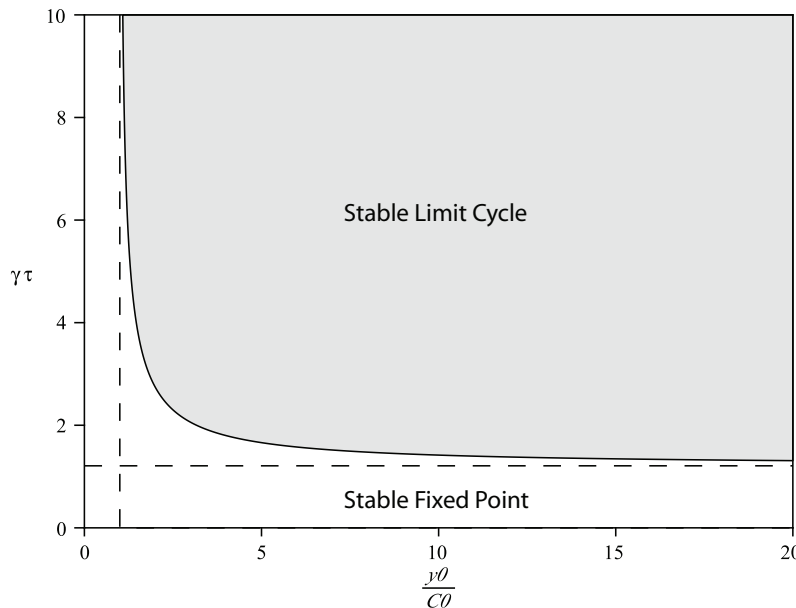
$$\frac{dy(t)}{dt} = \frac{K}{\left(1 + \frac{y(t-\tau)}{C_0}\right)^n} - \gamma y(t), \quad (6)$$



**Supplementary Figure 20:** Oscillation period versus [IPTG] for the negative feedback-only simulations shown in Supplementary Fig. 19.  $k_{\ell, \text{original}}$  is the value of  $k_{\ell}$  used in the dual-feedback model. As [IPTG] is scanned, the period varies less than what was seen experimentally in the dual-feedback system. For the  $k_{\ell} = 0$  case, oscillations in the deterministic model decay at [IPTG] > 0.2 mM and are only observed in stochastic simulations; therefore, we define the period as the maximum in the power spectrum of the stochastic trajectory.

with  $y(t)$  the amount of some repressor at time  $t$ ,  $K$  the unrepressed production rate,  $C_0$  an affinity constant, and  $\gamma$  a first-order degradation rate. Analytical results for such delayed negative feedback systems are well known (Bliss et al. 1982; Mackey and Nechaeva 1995; Bratsun et al. 2005), and we do not re-derive them here. If we define  $y_0$  to be the unique fixed point for Eq. 6, the bifurcation diagram can be represented in terms of the variables  $\gamma\tau$  and  $y_0/C_0$  (Supplementary Fig. 21). An important conclusion derived from this bifurcation diagram is that increasing the delay (for some fixed  $\gamma$ ) expands the region of parameter space in which the system exhibits stable oscillations. In this sense, increasing intracellular delay leads to enhanced robustness of stable oscillations in delayed negative feedback systems.

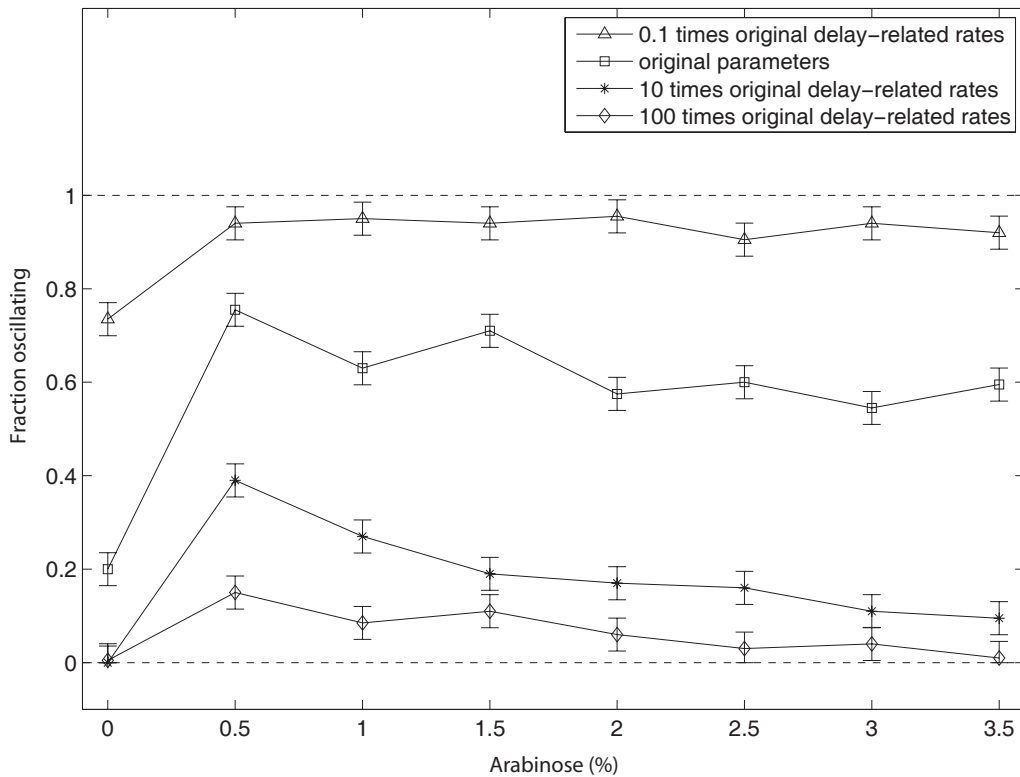
Although our full dual-feedback model contains richer dynamics than the delayed negative feedback model briefly described above, conceptual similarity between their basic mechanisms suggests that increasing delay will enhance robustness. The robustness of the full model was numerically explored by probing nearby parameter sets and determining if these sets display oscillatory behavior (see Supplementary Fig. 22 for details of the numerical analysis). One result of this numerical investigation is that the fraction of accessible parameter space (i.e. near the listed parameter values) exhibiting stable oscillations is above 50% for most points taken along the arabinose transect at 2 mM IPTG. This result should be contrasted to the exponentially small (in the



**Supplementary Figure 21:** The bifurcation diagram for the delayed negative feedback system. In this case,  $n = 2$ . The bifurcation boundary approaches the asymptotes (marked with dashed lines) defined by  $\gamma\tau = \arccos(-1/n)/\sqrt{n^2 - 1}$  and  $y_0/C_0 = 1/(n - 1)$ . Notice that the bifurcation boundary is monotonically decreasing in  $y_0/C_0$  with increasing  $\gamma\tau$ . Since  $y_0$  is independent of  $\tau$  (but not  $\gamma$ ), this monotonicity implies that the region of parameter space that supports stable oscillations monotonically increases with increasing  $\tau$  and fixed  $\gamma$ .

number of varied parameters) hypervolume that could be expected when multiple parameters must be accurately and independently tuned. A second result of this numerical investigation, which corroborates our discussion of the above minimal model, is the tendency for an increased robustness with increasing effective delay.

While we have not rigorously proven a general causal relation between delay and enhanced robustness of oscillations, the above analytic and numerical evidence suggests that such a relation holds when the core of a gene oscillator comprises a delayed negative feedback loop. There may be value in basing the designs of future synthetic gene oscillators on such a principle, particularly if methods arise that allow the engineering of a sharply distributed delay between transcription and feedback.



**Supplementary Figure 22:** A numerical investigation of the effect of changing intracellular delay on robustness. This was investigated by probing the nearby parameter space for oscillatory behavior. All parameters were randomly sampled independently and uniformly (in log-space) between half and double their listed values. This approach was chosen to avoid preferential treatment of a particular set of the 21 varied parameters (Gutenkunst et al. 2007):  $k_\ell$ ,  $k_{u\ell}$ ,  $b_a$ ,  $b_r$ ,  $\alpha$ ,  $t_a$ ,  $t_r$ ,  $k_{fa}$ ,  $k_{fr}$ ,  $k_{da}$ ,  $k_{-da}$ ,  $k_{dr}$ ,  $k_{-dr}$ ,  $k_t$ ,  $k_{-t}$ ,  $d_a$ ,  $d_r$ ,  $\gamma$ ,  $c_e$ ,  $\epsilon$ ,  $\lambda$ . Initial conditions consisted of all promoters in the looped state with two bound repressor proteins ("P<sub>L,2</sub>"), zero mRNA levels, and zero protein levels for all but folded monomeric forms ("a" and "r"), which were uniformly sampled between 0 and 500 for both activator and repressor. A computed trajectory was determined to not be oscillatory if, after a transient of 2000 min, the maximal variation in the number of folded monomeric activator ("a") was less than 0.1 in a subsequent 400 min of simulation. The plot displays the fraction of oscillatory states for varying levels of arabinose and 2.0 mM IPTG. This procedure was repeated for different mean values of certain delay-related rates, being done by multiplying the listed parameter values for the forward rates of folding, dimerization, and tetramerization by some common value (listed in the figure legend). Error bars were set to the maximum standard deviation  $\sigma_{max} = 0.5/\sqrt{N}$  for the average of  $N = 200$  Bernoulli trials. The data supports that decreasing the delay in the system tends to reduce the fraction of oscillatory states in nearby parameter space, while increasing delay has the opposite effect.

## References

- Andersen, J. B., Sternberg, C., Poulsen, L. K., Bjorn, S. P., Givskov, M. and Molin, S. (1998). New unstable variants of green fluorescent protein for studies of transient gene expression in bacteria. *Appl Environ Microbiol* 64:2240–2246.
- Atlung, T., Christensen, B. B. and Hansen, F. G. (1999). Role of the Rom protein in copy number control of plasmid pBR322 at different growth rates in *Escherichia coli* K-12. *Plasmid* 41:110–119.
- Baba, T., Ara, T., Hasegawa, M., Takai, Y., Okumura, Y., Baba, M., Datsenko, K. A., Tomita, M., Wanner, B. L. and Mori, H. (2006). Construction of *Escherichia coli* K-12 in-frame, single-gene knockout mutants: the Keio collection. *Mol Syst Biol* 2:2006.0008.
- Bendib, S. and Français, O. (2001). Analytical study of microchannel and passive microvalve “application to micropump simulator”. In *Design, Characterisation, and Packaging for MEMS and Microelectronics 2001*, pp. 283–91, Adelaide, Australia.
- Bliss, R. D., Painter, P. R. and Marr, A. G. (1982). Role of feedback inhibition in stabilizing the classical operon. *J Theor Biol* 97:177–193.
- Bratsun, D., Volfson, D., Tsimring, L. S. and Hasty, J. (2005). Delay-induced stochastic oscillations in gene regulation. *PNAS* 102:14593–14598.
- Chang, A. C. and Cohen, S. N. (1978). Construction and characterization of amplifiable multicopy DNA cloning vehicles derived from the P15A cryptic miniplasmid. *J Bacteriol* 134:1141–1156.
- Cookson, S., Ostroff, N., Pang, W. L., Volfson, D. and Hasty, J. (2005). Monitoring dynamics of single-cell gene expression over multiple cell cycles. *Mol Syst Biol* 1:msb4100032–E1–6.
- Cormack, B. P., Valdivia, R. H. and Falkow, S. (1996). FACS-optimized mutants of the green fluorescent protein (GFP). *Gene* 173:33–38.
- Datsenko, K. A. and Wanner, B. L. (2000). One-step inactivation of chromosomal genes in *Escherichia coli* K-12 using PCR products. *Proc Natl Acad Sci U S A* 97:6640–6645.
- Duffy, D. C., McDonald, J. C., Schueller, O. J. A. and Whitesides, G. M. (1998). Rapid prototyping of microfluidic systems in poly(dimethylsiloxane). *Anal Chem* 70:4974–84.
- Duffy, D. C., Schueller, O. J. A., Brittain, S. T. and Whitesides, G. M. (1999). Rapid prototyping of microfluidic switches in poly(dimethyl siloxane) and their actuation by electro-osmotic flow. *J Micromech Microeng* 9:211–7.
- Elowitz, M. B., Levine, A. J., Siggia, E. D. and Swain, P. S. (2002). Stochastic gene expression in a single cell. *Science* 297:1183–1186.
- Gillespie, D. T. (1977). Exact stochastic simulation of coupled chemical-reactions. *J Phys Chem* 81:2340–2361.

- Groisman, A., Lobo, C., Cho, H., Campbell, J. K., Dufour, Y. S., Stevens, A. M. and Levchenko, A. (2005). A microfluidic chemostat for experiments with bacterial and yeast cells. *Nat Methods* 2:685–9.
- Gutenkunst, R. N., Waterfall, J. J., Casey, F. P., Brown, K. S., Myers, C. R. and Sethna, J. P. (2007). Universally sloppy parameter sensitivities in systems biology models. *PLoS Comp Bio* 3:1871–1878.
- Kahn, M., Kolter, R., Thomas, C., Figurski, D., Meyer, R., Remaut, E. and Helinski, D. R. (1979). Plasmid cloning vehicles derived from plasmids ColE1, F, R6K, and RK2. *Methods Enzymol* 68:268–280.
- Lee, S. K., Chou, H. H., Pfleger, B. F., Newman, J. D., Yoshikuni, Y. and Keasling, J. D. (2007). Directed evolution of araC for improved compatibility of arabinose- and lactose-inducible promoters. *Appl Environ Microbiol* 73:5711–5715.
- Lutz, R. and Bujard, H. (1997). Independent and tight regulation of transcriptional units in *Escherichia coli* via the LacR/O, the TetR/O and AraC/I<sub>1</sub>-I<sub>2</sub> regulatory elements. *Nucleic Acids Res* 25:1203–1210.
- Mackey, M. C. and Nechaeva, I. G. (1995). Solution moment stability in stochastic differential-delay equations. *Phys Rev E* 52:3366–3376.
- Miller, J. H. (1992). *A short course in bacterial genetics*. Cold Spring Harbor Laboratory Press.
- Rateitschak, K. and Wolkenhauer, O. (2007). Intracellular delay limits cyclic changes in gene expression. *Math Biosci* 205:163–179.
- Shaner, N. C., Steinbach, P. A. and Tsien, R. Y. (2005). A guide to choosing fluorescent proteins. *Nat Methods* 2:905–909.
- Sheff, M. A. and Thorn, K. S. (2004). Optimized cassettes for fluorescent protein tagging in *Saccharomyces cerevisiae*. *Yeast* 21:661–670.
- Sia, S. K. and Whitesides, G. M. (2003). Microfluidic devices fabricated in poly(dimethylsiloxane) for biological studies. *Electrophoresis* 24:3563–76.
- Siegele, D. A. and Hu, J. C. (1997). Gene expression from plasmids containing the *araBAD* promoter at subsaturating inducer concentrations represents mixed populations. *Proc Natl Acad Sci U S A* 94:8168–8172.
- Tesla, N. (1920). U. S. Patent No. 1,329,559.
- Unger, M. A., Chou, H. P., Thorsen, T., Scherer, A. and Quake, S. R. (2000). Monolithic microfabricated valves and pumps by multilayer soft lithography. *Science* 288:113–6.
- Whitesides, G. M., Ostuni, E., Takayama, S., Jiang, X. and Ingber, D. E. (2001). Soft lithography in biology and biochemistry. *Annu Rev Biomed Eng* 3:335–73.
- Zacharias, D. A., Violin, J. D., Newton, A. C. and Tsien, R. Y. (2002). Partitioning of lipid-modified monomeric GFPs into membrane microdomains of live cells. *Science* 296:913–916.